공학박사학위논문

Structural change and rheology of colloidal gel under flow

유동하에서의 콜로이드 젤의 구조변화 및 유변학적 거동

2016 년 2 월

서울대학교 대학원
화학생물공학부

박준동

Abstract

Structural change and rheology of colloidal gel under flow

Jun Dong Park

School of Chemical and Biological Engineering

The Graduate School

Seoul National University

Colloidal particles are important in many fields of science and industry, because the properties of materials such as elasticity or electric conductivity can be dramatically tuned by colloidal particles. Mostly, the change of the material properties is attributed to the distinctive internal structure, which is formed by colloidal particles. A main example is a colloidal gel system. At sufficiently high concentration, colloidal particles that interact through attractive forces organize a space-filling percolated network structure, which is called colloidal gel. The gelation occurs in a wide range of colloidal particle system. Colloidal gel is characterized by solid-like behavior. The solid-like elastic property arises from the

disordered solid structure of the particles that are in the dynamically arrested state. Due to the formation of a microscopic network structure, colloidal gel shows a variety of complex properties that have not been fully understood yet.

When large deformation or stress is applied, colloidal gel undergoes a rupture of the network structure and flows in a strongly non-Newtonian manner, displaying many non-linear rheological behaviors. The rupture of the network structure is known as yielding. Yielding takes forms of various structural changes such as rearrangement, bond rupture, cage breakage, and structural anisotropy. Many experimental and theoretical approaches, ranging from light scattering to computer simulation, have been conducted to figure out the yielding behavior of colloidal gel. However, in spite of all these efforts, yielding of colloidal gel still leaves a lot of questions to be answered, especially about its fundamental mechanism.

The yielding behavior of colloidal gel which is represented by complex structural changes, especially the rupture of stress-bearing network structure, has an effect on the stress response of colloidal gel. The complex structural changes are manifested as nonlinear rheological behaviors, for example yield stress and non-linear creep compliances. Considering the close relationship between the microstructure and the rheological behavior, characterization of the structural change of colloidal gel is crucial in understanding the non-linear rheological behaviors. Therefore, the fundamental origins of non-linear rheological phenomenon have been commonly studied by investigating the coupling between the microstructural change and the rheological property. The coupling between the

microstructural change and the rheological property changes has been main issue in rheology.

Typically, the coupling between the microstructure and the rheology has been studied under the dynamic oscillatory shear flow and the start-up of shear flow. In experimental studies with these flow conditions, stress responses which are measured through rheometry have been correlated to the structural evolution that is analyzed through direct visualization and scattering methods. However, the analysis of the structural evolution is restricted to some specific conditions. In addition, there are many experimental difficulties, which make it hard to observe the structural changes. As an alternative to the limit of experimental study, theoretical study using particle simulation method can be suggested. Particle simulation has advantages over experiments to some extent, because all the information on the position of the particles and their interactions (such as forces and torques) can be correctly accessible. Among many simulation methods, the Brownian dynamics simulation has been widely used as a powerful tool to study colloidal particles system. The Brownian dynamics simulation has successfully depicted many important features of colloidal systems, such as colloidal gel and glass, which are dominated by particle interaction.

This work aims to study the coupling between the microstructural change and the rheological behavior of the colloidal gel by using the Brownian dynamics simulation method. The microstructural evolution and the dynamics of the colloidal gel will be studied under the start-up shear and the dynamic oscillatory shear flow.

Taking the advantage of the particle simulation method, which enables the investigation of all physical information on the particle position and dynamics, the structural change of colloidal gel will be investigated from various perspectives. The structural change and dynamics under various flow conditions will be analyzed through statistical mechanics and correlated to the rheological behavior. The result offers an insight into the yielding behavior of the colloidal gel and an interpretation on the relevant non-linear rheological behavior.

Key words: Colloidal gel, Start-up shear flow, Oscillatory shear flow, Yielding, Brownian dynamics simulation, SAOS (Small Amplitude Oscillatory Flow), MAOS (Medium Amplitude Oscillatory Flow), LAOS (Large Amplitude Oscillatory Flow), Structural anisotropy, stress-SANS rule.

Student Number: 2010-20991

Contents

List of Figures

Chapter 1. Introduction

1. Introduction

Colloidal particles form diverse microstructures depending on the interaction between the particles. Due to close relationship between microstructure and macroscopic material properties, theoretical and experimental studies have been conducted to explore various microstructures of the colloidal systems. At low volume fraction, colloidal particles may form fractal aggregates. As the volume fraction increases, the aggregates organize a percolated network structure, colloidal gel. The structure and physical properties of the colloidal gel observed at low volume fraction has often been studied by fractal concept [1-4]. On the other hand, at high volume fraction, they can form a closely packed structure, which is called colloidal glass. Mode Coupling Theory (MCT) adopting cage concept has been used to describe the nature of the colloidal glasses [5-7]. In between the two cases of fractal gel at low volume fraction and colloidal glass at high volume fraction, the structure and the physical properties of colloidal gel at intermediate volume fraction $(\geq 10\%)$ have been studied through a variety of approaches [8-12]. However, colloidal gel at intermediate volume fraction still leaves unanswered questions about its complex structure and physical properties.

A colloidal gel at intermediate volume fraction, which will be handled in this work, is characterized by a sample-spanning network structure of dynamically-arrested particles [13-14]. The network structure of the colloidal gel imparts solid-like elastic properties which result in complex rheological behavior. In many studies, using theoretical [15-17], experimental, and simulation approaches [18-20], the origin of the elasticity has been studied and correlated to the microstructure of the stress-bearing networks. Topological analysis of the colloidal gel demonstrates that the stress-bearing network consists of dynamically arrested particles with high coordination number or bond number. These works suggest a strong correlation between the elasticity and the microstructure. Recently, a numerical study on the aging of colloidal gel gives an insight into the relationship between the elasticity

and microstructure [21]. In addition, experimentally, a model gel system has been studied for coordinated measurements of structure and rheology, which is expected to enable more quantitative experimental analysis [22].

Under the conditions of the sufficiently large deformation or stress, the colloidal gel undergoes rupture of microstructure. This structural rupture is called yielding. The yielding is manifested by various structural changes such as rearrangement, bond rupture, cage breakage, and flow-induced anisotropy [20, 23-26]. Depending on the conditions, the colloidal gel shows diverse yielding mechanism. The fractal gels at low volume fraction demonstrate the yielding process of structural reorientation, break-up, and cluster densification under the step shear [27]. In between the two cases of fractal gel at low volume fraction and dense gel at high volume fraction, the colloidal gel at intermediate volume fraction shows a yielding behavior in the sequence of deformation, breakup of the percolated network structure, rotation and breakup of the clusters, and equilibration of the three representative motions of small flocs [20]. At intermediate volume fraction, a new perspective, which regards the yielding of colloidal gel as a transition from rigid chain to soft chain, has been suggested [22]. In a recent study under the step shear [28], the yielding of the colloidal gel at intermediate volume fraction has been studied in terms of the stress localization and stiffening, which corresponds to stretching and alignment of the network chains. On the other hand, studies under oscillatory shear show two-step yielding behavior. At low concentration, the colloidal gel shows two-step yielding, which is caused by bond rotation and bond breakage [29]. In the case of dense gel at high volume fraction, another two-step yielding behavior of bond breakage and cage breaking has been suggested [25]. Despite all these efforts, the yielding of a colloidal gel is not fully understood yet.

The yielding behavior, which is caused by the applied deformation or stress, accompanies linear to non-linear transition of the rheological properties [19,20]. This coupling between microstructural change and rheological property changes of colloidal gel has been investigated mainly under the start-up of shear flow. The colloidal gel under the start-up shear flow has been studied using direct

visualization [19], light scattering [27], and simulation method [20, 30-31]. In these studies, the dynamics of colloidal gels were investigated by analyzing the structural evolution under the start-up of shear flow, which directly led to a correlation between the microstructure and rheology. The study using light scattering was limited to relatively low volume fraction, because experimental difficulties such as multiple scattering were encountered, which made it hard to investigate the structural evolution as the concentration increased. Due to these experimental difficulties, the structural evolution of colloidal gel at intermediate volume fraction has rarely been fully investigated. As an alternative, direct visualization methods with 2-dimensional suspension which gives high temporal and spatial resolution were conducted [8, 26, 27]. From these studies, using 2-dimensional model colloidal gel, flow-induced structure was investigated by varying the surface coverage and shear rate. Direct observation of the structural change of colloidal gel provided valuable clues about its structural evolution, but there still remains question on the possible application to 3-dimensional space due to the limitation of 2-dimensional space (interface between two heterogeneous materials). Recently, fast confocal microscopes and photopolymerization techniques have allowed investigation on the 3-dimensional morphology of sheared gels, enabling more detailed understanding on microstructural changes [24, 28]. However, the fast confocal microscope techniques are still applicable to some restricted system.

Under shear flow, structural anisotropy is another important manifestation of yielding. The structural anisotropy has been studied extensively through scattering methods. In preceding works, the structural anisotropy under steady shear flow was studied through flow-SANS [32] and light scattering [33]. In another work [34], the structural anisotropy was probed across a broad range of length scales utilizing small angle light scattering (SALS), small angle x-ray scattering (SAXS), and ultra-small angle x-ray scattering (USAXS). These results revealed structural anisotropy along the vorticity axis, which is characterized by butterfly pattern in the velocity-vorticity plane. Lately, by virtue of newly developed sample environment for SANS under flow, the structural anisotropy was studied on the

shorter length scale corresponding to local microstructure [35, 36]. In these works, microstructural change corresponding to particle length scale was studied in both the velocity-vorticity plane and the velocity-gradient plane. In addition to the butterfly pattern in the velocity-vorticity plane, colloidal gel demonstrates structural anisotropy along the compressional axis, which is represented by enhanced scattering pattern along the extensional axis. Apart from the experimental works using scattering, the structural anisotropy of colloidal gel has been researched through a variety of approaches. Different from the scattering works, where the structural anisotropy is analyzed in reciprocal space, direct visualization using microscopy [8, 37] makes it possible to study structural anisotropy in real space. Correlating structural anisotropy to directional dependent dynamics of the aggregates, the previous work supports our understanding on flow-induced structural anisotropy. Although the structural anisotropy of the colloidal gel has been well studied, there is still lack of understanding on the mechanism leading to structural anisotropy. Especially, compared with the structural anisotropy along compressional direction, there is relatively limited understanding on the origin of structural anisotropy along vorticity direction. Lately, an outstanding work [38] has elucidated the role of hydrodynamic interaction and confinement in formation of anisotropic structure along the vorticity direction. However, influence of attractive interaction, which affects dominantly in colloidal gel system, is still remained as unsolved problem. Moreover, the coupling between structural anisotropy and rheology has not been studied sufficiently yet. Previous study on the structural anisotropy-rheology relationship is limited to the colloidal gel at low volume fraction [27] and there is insufficient quantitative study on colloidal gel, which directly correlates the structural anisotropy to rheological behavior.

The coupling between the microstructure and rheology of colloidal gel has been studied with the dynamic oscillatory shear flow as well as with the start-up shear flow. In the studies using dynamic oscillatory shear flow, the coupling between the microstructure and rheology was analyzed by investigating the changes in rheological properties. In the example at the top, two-step yielding [25,29]

mechanism has been suggested according to the change of G′ and G″. However, the change of G′ and G″ is not enough to clearly describe the behavior of colloidal gels. Moreover, G′ and G″ are defined under the assumption of a linear response. Thus, they are not appropriate to explain yielding behavior of colloidal gel that accompanies nonlinear stress responses [40]. Additionally, the absence of information on the microstructural change makes it hard to understand the stress response of colloidal gels. Lately, Rheo-SANS has been used to study the microstructure under the dynamic oscillatory shear flow and showed a link between the microstructural change and the rheological behavior [36, 40]. However, rheo-SANS gives information only on the averaged microscopic dynamics. The structural change of a colloidal gel under oscillatory shear flow has also been observed by confocal microscopy [41]. However, it was confined to the static structure after oscillatory shear flow rather than the dynamic structural changes during the oscillatory shearing. Considering that the nonlinear response is more closely connected to the dynamic structural changes during the oscillatory shear flow rather than the static structure after the flow, understanding the dynamics of colloidal gels cannot be achieved without grasping the oscillating dynamics. Therefore, there is a need of study on the oscillating dynamics of colloidal gels. In addition, the dependence of nonlinear responses and microstructural changes on various oscillatory shear flows should be studied further and discussed with consideration of the oscillating dynamics.

In this work, we investigate the microstructural changes and the rheological behavior of colloidal gel under start-up shear flow and dynamic oscillatory shear flow using the Brownian dynamics simulations. Firstly, the structural evolution of the colloidal gel under the start-up shear is investigated. The structural evolution is analyzed in two different length scales (cluster length scale and local length scale) and in terms of structural anisotropy. The observed structural evolution is correlated to the stress overshoot behavior to elucidate the relationship between microstructural change and rheological behavior. Secondly, the structural

anisotropy of colloidal gel under start-up shear flow is investigated more intensively. The result provides fundamental explanation on the structural anisotropy inducing mechanism. In addition, the structural anisotropy is linked to the stress response via a stress-SANS rule, which is modified from the original stress-SANS rule to consider the influence of the structural change of the colloidal gel. Lastly, the structural change and dynamics of colloidal gel under oscillatory shear flow are investigated. The microstructural change of the colloidal gel under various oscillatory shear conditions (strain amplitude and frequency) is studied. Depending on the conditions, the colloidal gel presents different microstructures, which manifest themselves with different oscillating dynamics and stress responses. The oscillating dynamics and rheological behavior are explored in three flow regimes of different strain amplitudes; SAOS (small amplitude oscillatory shear), MAOS (medium amplitude oscillatory shear), and LAOS (large amplitude oscillatory shear) regimes. Based on the results, the coupling between the microstructural change, dynamics and rheological behavior is discussed.

Chapter 2. Theory

2.1. Brownian Dynamics simulation with surface bonding Model

In a three dimensional cubic box, 10,000 particles were placed to form a weakly aggregating colloidal gel (15 or 20 volume %). Lee-Edwards boundary condition was applied [42]. At every time step, the position of each particle was updated according to the Langevin equation [43]. The hydrodynamic force was approximated by simple Stokesian drag, and the hydrodynamic interaction was not considered in this simulation. The Brownian motion was described by stochastic displacement induced by the Gaussian random force.

The governing equations were formulated in terms of dimensionless parameters. The length was scaled by the radius (a) of the particle, and the energy by the thermal energy $(k_B T)$. The time was scaled with the characteristic time (τ_r) during which the particles diffuse the radius of a particle (a).

$$\tau_r = \frac{a^2}{D^T}. \tag{2.1}$$

Here, D^T is the translational diffusion coefficient of the particle at infinite dilution,

Using the characteristic time (τ_r), the Peclet number, which represents the ratio of shear force to Brownian force, was defined as,

$$Pe = \dot{\gamma}\tau_r \tag{2.2}$$

to describe the extent of shear flow. In the simulation, the time step (Δt) was set to 10^{-5}, small enough to prevent drastic change of the particle position and the inter-particle force at high Peclet number.

In this work, the concept of surface bonding was introduced to the Brownian dynamics simulation [44]. When two particles come close within a bonding distance, bond nodes are formed on the particle surface, which are the intersection points of the particle surfaces and a line connecting the particle centers. Between the bond nodes, a flexible surface-to-surface bond is formed. The presence of the surface bond can be an index to judge whether the particles are connected or not. This bond describes non-central attractive interaction between the particles until it exceeds the maximum bond length $(b_{\max})$ after which the bond breaks-up. Considering the rotational motion of the particles and restricting the angular reorganization of the particles, the surface-to-surface bonding concept describes the colloidal system accurately [30]. Details of the Brownian dynamics simulation with the concept of surface bonding are described elsewhere [44]. Here, we briefly explain the particle interaction, bonding scheme and simulation algorithm.

2.1.1. Particle interaction & bonding scheme

The potential to describe the interaction between the particles consists of three sorts of potentials: core potential (ϕ_C), bonding potential (ϕ_B), non-bonded long range potential (ϕ_N). The core potential, which characterizes the particle surface, was given as a very steep repulsive potential to prevent the overlap of the particles.

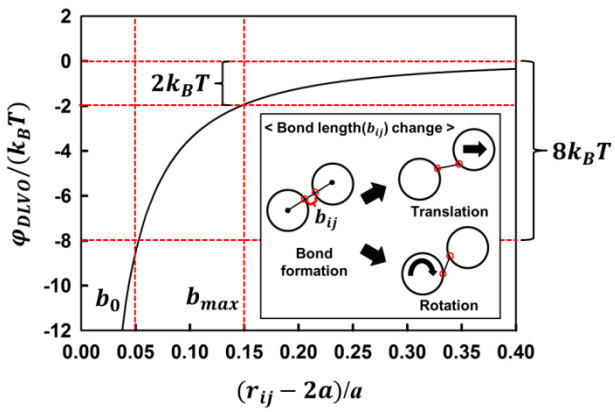

Figure. 2.1.1. DLVO potential of the present particle system (a=1μm, $A = 3.2 \times 10^{-20}$J, $\varepsilon = 81\varepsilon_0$ F m^{-1}, $\psi = 4$mV, $\kappa = 5 \times 10^7\ m^{-1}$). Bond formation and length change mechanism (Inset).

$$\begin{aligned}\phi_C\left(r_{ij}\right) &= \frac{1}{2}K\left(2a - r_{ij}\right)^2, r_{ij} < 2a \\ &= \quad 0 \quad\quad , r_{ij} \geq 2a\end{aligned} \tag{2.3}$$

Here, r_{ij} is the inter-particle distance defined as

$$r_{ij} = \left|\boldsymbol{r_i} - \boldsymbol{r_j}\right| \tag{2.4}$$

The potential energy parameter $\left(K\right)$ was set to 4000, high enough to result in an overlap of less than 0.5% of the total particles at each time step.

When two particles come close within a critical distance $\left(r_{ij} < 2.15a\right)$, a bond is formed on the particle surface and it describes the non-central inter-particle attractive interaction. Once the bonds are formed on the particle surface, the forces and the torques induced by these bonds result in translational and rotational motion of the particles. The structural change by the motions of the particles leads to the change of the bond length as depicted in the inset of Figure. 2.1.1. Many of the preceding researches assumed the bond as the bead-spring chain (Hookean spring), which has been widely used in polymer dynamics [30, 31, 44, 45]. However, it is less realistic in colloidal system which show significant differences [17]. Therefore, to describe the particle interaction more realistically, we used DLVO (Derjaquin, Landau, Verwey, Overbeek) potential to describe the bonds between the particle surfaces [46]. The bonding potential and the bonding scheme were adjusted according to the calculated inter-particle potential. The DLVO potential was given in the form;

$$\varphi_{DLVO}\left(r_{ij}\right) = \varphi_{vdW}\left(r_{ij}\right) + \varphi_{el}\left(r_{ij}\right) \tag{2.5}$$

$$\varphi_{vdW}\left(r_{ij}\right) = -\frac{A}{6}\left[\frac{2a^2}{r_{ij}^{\ 2} - 4a^2} + \frac{2a^2}{r_{ij}^{\ 2}} + \ln\left(\frac{r_{ij}^{\ 2} - 4a^2}{r_{ij}^{\ 2}}\right)\right] \tag{2.6}$$

$$\varphi_{el}\left(r_{ij}\right)=\frac{\varepsilon a\psi^{2}}{2}\left[\ln\left(1+\exp\left(-\kappa\left(r_{ij}-2a\right)\right)\right)\right] \tag{2.7}$$

where $A,\varepsilon,\psi,\kappa$ represent the Hamaker constant, dielectric constant of solvent, surface potential of the particle, and Debye screening length, respectively.

Depending on the bond length between the particle surfaces (b_{ij}), the bonding potential is divided into two parts using b_0 (stable region parameter) and $b_{\max}$ (maximum bond length) as criteria.

$$\begin{aligned}\phi_B\left(b_{ij}\right)&=\varphi_{DLVO}\left(b_0+2a\right) \quad , \quad b_0\geq b_{ij}\\ &=\varphi_{DLVO}\left(b_{ij}+2a\right) \quad , \quad b_{\max}\geq b_{ij}>b_0\end{aligned} \tag{2.8}$$

For the bond whose length is less than b_0, the bonding potential was set to a constant value of $\varphi_{DLVO}\left(b_0+2a\right)$ to describe the stable region where no attractive force is assumed. On the other hand, for the bond which has length longer than b_0 and shorter than maximum bond length$\left(b_{\max}\right)$, the bond was described as a spring with a DLVO potential. According to the calculated DLVO potential in Figure. 2.1.1 and assumption of the weakly aggregating colloidal gel, we assumed b_0 to be $0.05a$, where the potential well depth becomes $8\mathrm{k_B}T$. The maximum bond length $\left(b_{\max}\right)$ was set to be $0.15a$ where the inter-particle potential becomes twice of the thermal energy $\left(-2k_BT\right)$ as shown in Figure. 2.1.1.

As the particles are separated from each other, the bond $\left(b_{ij}\right)$ exceeds the maximum bond length $\left(b_{\max}\right)$ and breaks-up. After the break-up, the particle interaction is described by non-bonded long range interaction$\left(\phi_N\left(r_{ij}\right)\right)$, without interaction by surface bonds. In this work, this center-to-center inter-particle potential was set as the DLVO potential.

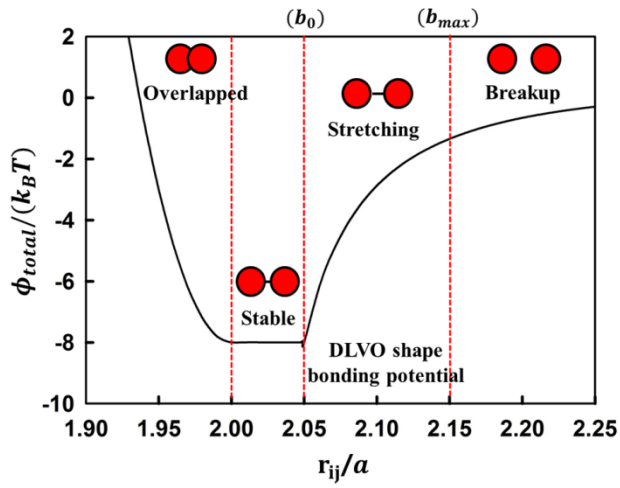

Figure. 2.1.2. Pair interaction potential for a collinear extension.

$$\phi_N\left(r_{ij}\right)=\varphi_{DLVO}\left(r_{ij}\right) \tag{2.9}$$

Putting three potentials altogether, the total inter-particle potential is represented by a function of the inter-particle distance and the bond length as follows. Differentiating the total inter-particle potential, we can get the total inter-particle force $\left(\mathbf{F_{ij}}\right)$, by which the particle position is updated.

$$\begin{aligned}\phi_{total}&=\phi_c\left(r_{ij}\right)+\phi_B\left(b_{ij}\right)+\phi_N\left(r_{ij}\right)\\ \boldsymbol{F_{ij}}&=-\nabla\phi_{total}\left(r_{ij},b_{ij}\right)\end{aligned} \tag{2.10}$$

In Figure. 2.1.2, pair interaction potential for a collinear extension, in which the bond length $\left(b_{ij}\right)$ coincides with the surface separation $\left(r_{ij}-2a\right)$, is plotted. If the particles are overlapped $\left(2a>r_{ij}\right)$, they repel each other by the strong repulsive force induced from the core potential $\left(\phi_c\left(r_{ij}\right)\right)$. At a stable region, the potential is set to a constant $\left(\varphi_{DLVO}\left(b_0+2a\right)\right)$ implying no inter-particle force between them. As the particles are separated from each other, the bond length $\left(b_{ij}\right)$ exceeds b_0 and the bonding potential of DLVO shape $\left(\phi_B\left(b_{ij}\right)\right)$ begins to describe the attractive interaction between the two particles until the bond length reaches the maximum value $\left(b_{\max}\right)$. Exceeding the maximum bond length, the bond on the particle surface breaks-up and the particle interaction is governed by non-bonded long range interaction $\left(\phi_N\left(r_{ij}\right)\right)$.

2.1.2. Simulation algorithm

The translational motion of the particle is described by the Langevin equation [43].

$$m\frac{d\boldsymbol{v}_i(t)}{dt} = -\xi\boldsymbol{v}_i(t) + \sum_j \boldsymbol{F}_{ij}(t) + \boldsymbol{F}_i^R(t) \tag{2.11}$$

Here, the first term on the right-hand side represents the hydrodynamic force. Because we ignored hydrodynamic interaction, Stokes friction coefficient $\xi(=6\pi\eta a)$ was used to describe the hydrodynamic force experienced by the fluid. The second term is the inter-particle interaction explained in the previous section, and the last term is the random force representing the thermal fluctuation of the particles. This random force gives uncorrelated displacement of $\sqrt{2D^T dt}$ for each direction (x, y, z) on average, where D^T is the translational diffusion coefficient. In this work, the relaxation time of the particle motion (m/ξ) was assumed to be very small, and the inertia term on the left was ignored. Assuming shear flow as a linear profile, the above Langevin equation could be discretized as follows by the Euler method.

$$\boldsymbol{r}_i(t+\Delta t) = \boldsymbol{r}_i(t) + \left[\sum_j \boldsymbol{F}_{ij}(t) + \boldsymbol{F}_i^R(t)\right]\frac{\Delta t}{\xi} + y_i\dot{\gamma}_{xy}\Delta t \tag{2.12}$$

The rotational motion of the particle is governed by the following equation

$$\Delta\boldsymbol{\varphi}_i = \left(\frac{\boldsymbol{T}_i}{\xi_R} + \frac{\boldsymbol{T}_i^R(D^R,t)}{\xi_R}\right)\Delta t \tag{2.13}$$

where $\Delta\boldsymbol{\varphi}_i$ is the total angular displacement and $\boldsymbol{T}_i, \boldsymbol{T}_i^R(D^R,t), \xi_R$ represent the inter-particle torque, the random torque by the rotational diffusion, and the rotational friction coefficient, respectively. The inter-particle torque $\boldsymbol{T}_i(t)$ induced by the particle-particle interaction could be calculated by

$$\boldsymbol{T}_\mathbf{i} = \sum_j \boldsymbol{a}_j \times \boldsymbol{F}_{ij}(t) \tag{2.14}$$

where $\boldsymbol{a}_j$ is the position of *j*-th bond on the surface of *i* particle relative to the *i* particle center. As we neglected multi-body hydrodynamic interaction, the rotational friction coefficient could be given by

$$\xi_R = 8\pi\eta a^3 . \tag{2.15}$$

The rotational diffusion of the particle was represented by the random torque. In this process, the magnitude of the random torque is given by

$$\left|\boldsymbol{T}^R\right| = \left|\frac{\Delta\boldsymbol{\varphi}^R \xi_R}{\Delta t}\right| \tag{2.16}$$

where $\Delta\boldsymbol{\varphi}^R$ is the random angular displacement by the rotational diffusion with the average of zero and the variance of $6D^R\Delta t$ (here, D^R is the rotational diffusion coefficient). In addition, the direction of the random torque was given randomly following the Marsaglia algorithm [43].

In order to measure the rheological properties of the colloidal gel, we calculated the stress under shear flow. It is often calculated from the Kirkwood form of the stress tensor [47]. However, in this work, as the torque exists due to the non-central force by the surface bonds, anti-symmetric stress associated with the vortex viscosity was inevitably included in the total stress tensor. As the macroscopic rheological quantities are related to the symmetric part of the stress only, not to the anti-symmetric part, we calculated the symmetric part by

$$\sigma_{\alpha\beta}{}^{sym} = -\frac{1}{2V}\left(\sum_{i=1}^{N}\sum_{j>i}^{N} r_{\alpha ij}F_{\beta ij} + \sum_{i=1}^{N}\sum_{j>i}^{N} r_{\beta ij}F_{\alpha ij}\right) \tag{2.17}$$

where α, β represent the Cartesian component of the vector quantities [43, 48]. Only a symmetric part of the total stress will be discussed in this work.

2.2. Structure analysis method

In this work, structural change of the colloidal gel is studied through pair distribution function, $g(\vec{\mathbf{r}},\gamma)$, and structure factor, $S(\vec{\mathbf{q}},\gamma)$. The pair distribution function and the structure factor measure the probability of finding particle at relative position of $\vec{\mathbf{r}}$ in real space and $\vec{\mathbf{q}}$ in reciprocal space at strain γ. Here, the pair distribution function and the structure factor are given by

$$g(\vec{\mathbf{r}},\gamma) = \frac{V}{N^2}\langle \sum_i \sum_{j\neq i} \delta\left(\vec{\mathbf{r}} - \vec{\mathbf{r}}_{ij}\right)\rangle \quad \text{at strain } \gamma \tag{2.18}$$

$$S(\vec{\mathbf{q}},\gamma) = 1 + \frac{1}{N}\langle \sum_i \sum_{j\neq i} \exp\left(-i\,\vec{\mathbf{q}}\cdot\vec{\mathbf{r}}_{ij}\right)\rangle \text{ at strain } \gamma \tag{2.19}$$

where N,V, $\vec{\mathbf{q}}$ represent number of the particles, volume of the simulation box and wave vector, respectively. To study the structural change during start-up shear flow quantitatively, we investigated the pair distribution function difference and the structure factor difference between transient state $(\gamma \neq 0)$ and quiescent state $(\gamma = 0)$. Figure. 2.2.1 shows the calculation of the pair distribution function difference and the structure factor difference. The second figures in Figure. 2.2.1.A and Figure. 2.2.1.B demonstrate the pair distribution function $\left(g(\vec{\mathbf{r}},0)\right)$ and the structure factor $\left(S(\vec{\mathbf{q}},0)\right)$ at quiescent state. At the quiescent state, both pair distribution function and structure factor show isotropic structure. The first figures of Figure. 2.2.1.A and Figure. 2.2.1.B display pair distribution function $\left(g(\vec{\mathbf{r}},\gamma)\right)$ and structure factor $\left(S(\vec{\mathbf{q}},\gamma)\right)$ calculated at transient state $(\gamma = 1)$. At transient state, the pair distribution function and the structure factor exhibit distortion and intensity change which can be attributed to the shear-induced structural change. The last figures of Figure. 2.2.1.A and Figure. 2.2.1.B demonstrate the pair distribution function difference $\Delta g(\vec{\mathbf{r}},\gamma)$, and structure factor difference $\Delta S(\vec{\mathbf{q}},\gamma)$, which is defined as

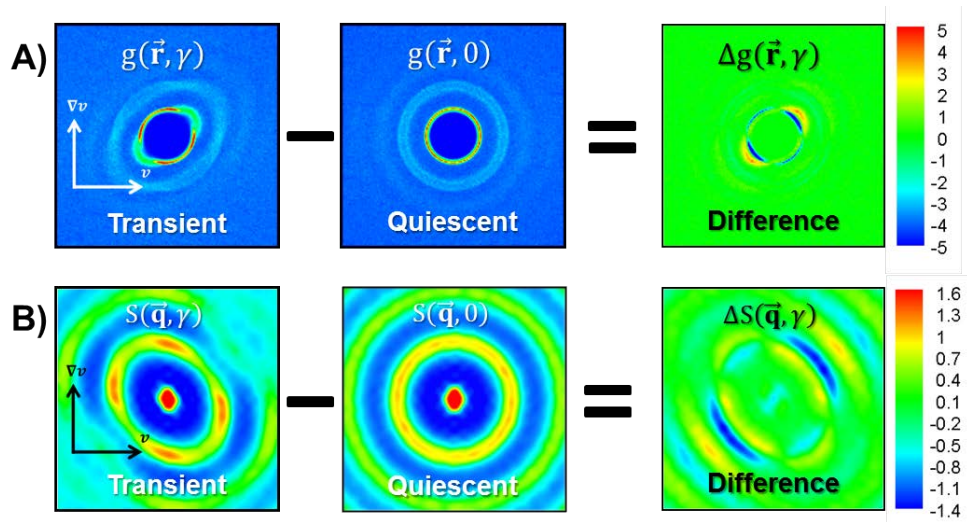

Figure. 2.2.1. Calculation of pair distribution function difference, $\Delta\mathbf{g}(\vec{\mathbf{r}},\boldsymbol{\gamma})$ and structure factor difference, $\Delta\mathbf{S}(\vec{\mathbf{q}},\boldsymbol{\gamma})$.

$$\Delta g(\vec{\mathbf{r}}, \gamma) = g(\vec{\mathbf{r}}, \gamma) - g(\vec{\mathbf{r}}, 0) \tag{2.20}$$

$$\Delta S(\vec{\mathbf{r}}, \gamma) = S(\vec{\mathbf{q}}, \gamma) - S(\vec{\mathbf{q}}, 0) \tag{2.21}$$

The differences, $\Delta g(\vec{\mathbf{r}}, \gamma)$ and $\Delta S(\vec{\mathbf{q}}, \gamma)$, effectively describe the structural changes from quiescent state, making it easier to distinguish the structure formation and breakup.

In Figure. 2.2.1, it is shown that the pair distribution function and the structure factor, which are isotropic at quiescent state, demonstrate anisotropy under shear flow due to shear-induced non-equilibrium structure. This indicates that the pair distribution function should not be treated as a function of the distance r to get the information on the anisotropy. Therefore, we expanded the pair distribution function $g(\vec{\mathbf{r}}, \gamma)$ in spherical harmonics to analyze the anisotropic non-equilibrium structure. The pair distribution function can be expanded in terms of spherical harmonics $Y_{lm}(\hat{\mathbf{r}})$ as

$$g(\vec{\mathbf{r}}) = g_s(r) + \sum_{l=1}^{\infty} \sum_{m=-l}^{l} g_{lm}(r)\, Y_{lm}(\hat{\mathbf{r}}). \tag{2.22}$$

The scalar contribution $g_s(r)$ is

$$g_s(r) = \frac{1}{4\pi} \int g(\vec{\mathbf{r}})\, d\hat{\mathbf{r}} \tag{2.23}$$

and the expansion coefficients are given by

$$g_{lm}(r) = \int Y_{lm}(\hat{\mathbf{r}}) g(\vec{\mathbf{r}})\, d\hat{\mathbf{r}} \tag{2.24}$$

Here, $\hat{\mathbf{r}}$ denotes $\vec{\mathbf{r}}/r$.

For a fluid subjected to plane Couette flow, using Cartesian irreducible tensors, this spherical harmonic expansion can be further simplified as follows [49]

$$\begin{aligned} g(\vec{\mathbf{r}}) &= g_s(r) + \sum_l \sum_k g_k^l\, X_k^l\, (\hat{\mathbf{r}}) \\ &= g_s(r) + g_0^2 X_0^2 + g_1^2 X_1^2 + g_2^2 X_2^2 + g_0^4 X_0^4 + g_1^4 X_1^4 + g_2^4 X_2^4 + \cdots \end{aligned} \tag{2.25}$$

where $X_k^l(\hat{\mathbf{r}})$ is given as

$$X_0^2 = \hat{z}^2 - \frac{1}{3}$$

$$X_1^2 = \frac{1}{2}(\hat{x}^2 - \hat{y}^2)$$

$$X_2^2 = \hat{x}\hat{y} \tag{2.26}$$

for rank 2. In Eq. (2.26), $\hat{x}, \hat{y}, \hat{z}$ are the components of $\hat{\mathbf{r}}$. The X_k^l terms are closely connected to the spherical harmonics terms Y_{lm}. In the case of even k, X_k^l is proportional to $\mathrm{Im}Y_{lk}$ and for odd k, X_k^l is proportional to $\mathrm{Re}Y_{lk+1}$. For zero k, X_k^l is proportional to Y_{l0}. The expansion coefficient g_k^l is

$$\mathrm{g}_k^l(r) = (\xi_l)^2 C_k^l \left(\frac{1}{4\pi}\right) \int X_k^l(\hat{\mathbf{r}}) \mathrm{g}(\vec{\mathbf{r}})\, d\hat{\mathbf{r}} \tag{2.27}$$

where ξ_l and C_k^l are

$$\xi_l = [(2l+1)!!/l!]^{1/2}$$

$$C_0^2 = \tfrac{3}{2}, C_1^2 = C_2^2 = 2. \tag{2.28}$$

By comparing the expansion coefficients g_k^l which indicate degree of the structural anisotropy related to each Cartesian irreducible tensor terms X_k^l, the shear-induced anisotropic structure of the colloidal gel under start-up shear can be analyzed quantitatively.

In the case of structure factor $\mathrm{S}(\vec{\mathbf{q}}, \gamma)$, the degree of structural anisotropy is characterized by the alignment factor, A_f [50]

$$A_f = \frac{\int_0^{2\pi} I(q^*, \phi, \gamma) \cos\big(2(\phi - \phi_0)\big) d\phi}{\int_0^{2\pi} I(q^*, \phi)\, d\phi} \tag{2.29}$$

where $I(q^*, \phi, \gamma)$ denotes the angular scattering intensity averaged over a q-range of $q^*(2.8a^{-1} \le q \le 3.6a^{-1})$ corresponding to the local structure of $2a$ length scale. Here, ϕ and ϕ_0 are the azimuthal angle relative to x-axis and the average orientation of the local structure, which is given by the minimum of $I(q^*, \phi, \gamma)$.

The alignment factor A_f, which is commonly used in scattering data analysis, indicates the degree of alignment of the structure about the ϕ_0. In scattering analysis, the scattering intensity $I(\vec{\mathbf{q}}, \gamma)$ is given by

$$I(\vec{\mathbf{q}}, \gamma) = p(\vec{\mathbf{q}}) \times \mathrm{S}(\vec{\mathbf{q}}, \gamma) \tag{2.30}$$

where p is the form factor of the particles. In this work, the form factor of the particles is assumed to be 1. Therefore, in Eq. (2.30), the structure factor $\mathrm{S}(\vec{\mathbf{q}}, \gamma)$ is used to calculate the alignment factor, A_f, instead of the scattering intensity $I(\vec{\mathbf{q}}, \gamma)$.

Chapter 3. Structural evolution of colloidal gel under start-up shear flow

3.1. Simulation system

At first, the particles were randomly placed in the simulation box (15% volume fraction). In the equilibration process, the particles moved randomly by the thermal motion. After enough time steps of order 10^6, about 70~80% of the total particles were aggregated to form a percolated network structure, which is the colloidal gel. To confirm the gel formation, we checked the fractal dimension and the bond number distribution. The fractal dimension $\left(D_f\right)$ was obtained by measuring the average number of the particles $\left(n\right)$ within a test range r

$$n \propto \tilde{n} r^{D_f} \tag{3.1}$$

where $\tilde{n}$ is the proportionality constant [51,52]. In Figure. 3.1.1, the fractal dimension was measured to be 2.4 from the slope of the plot. Simulation was conducted for five times with different initial particle configuration and random motion. This result implies that the colloidal gel formed in this simulation has an open structure of fractal-like aggregates. To check the topology of the colloidal gel, the initial bond number distribution $\left(P\left(z,\gamma=0\right)\right)$ was calculated in Figure. 3.1.2, according to which most particles were connected with 3 or 4 bonds. Thus, the colloidal gel in this simulation consists of multiply-connected rigid chains which are the origin of the elasticity [17, 18, 53, 54].

Figure. 3.1.3 shows the stress growth as a function of strain when the shear flow was applied. The stress increased up to a maximum and then decreased to a steady value. The stress overshoot should be related with the structural evolution that occurs during the rupture process by the shear flow [26, 55, 56]. For the viscoelastic materials like polymer gel or colloidal gel, the stress overshoot was commonly observed, and it was already reported in the previous studies using

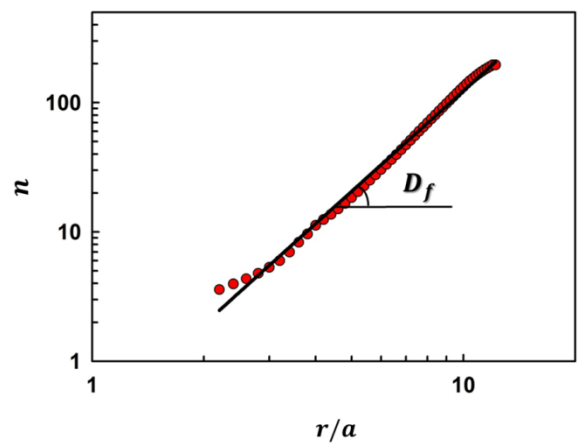

Figure. 3.1.1. Average number of particles (n) within a range r.

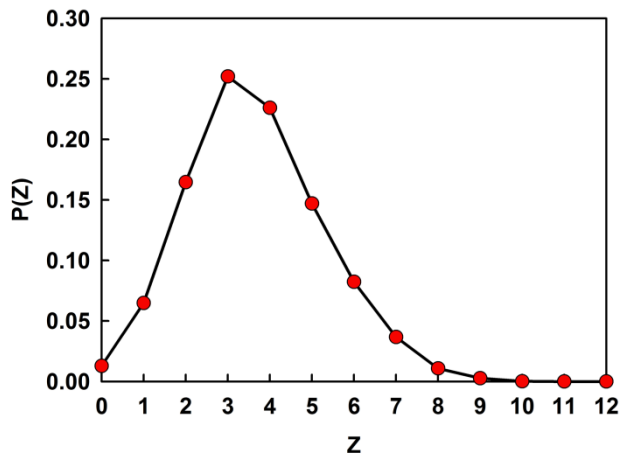

Figure. 3.1.2. Initial bond number distribution $P(z,0)$

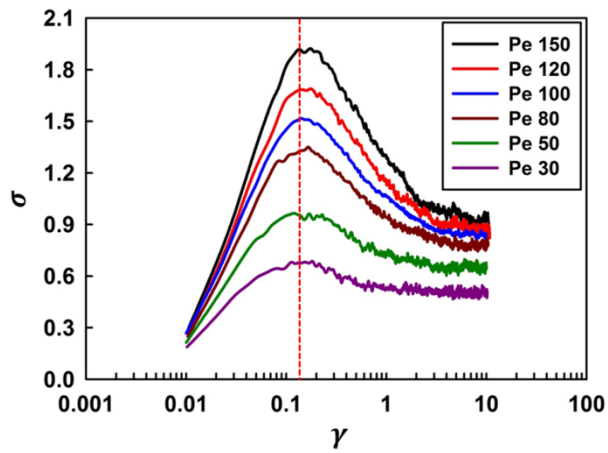

Figure. 3.1.3. Stress (σ) growth as a function of strain at various Pe.

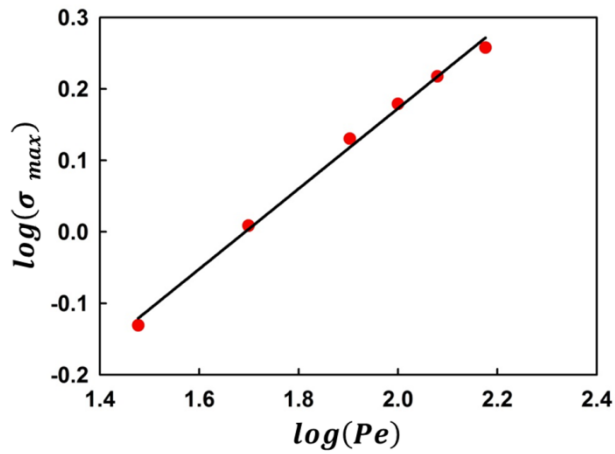

Figure. 3.1.4. Stress maximum $\left(\sigma_{\max}\right)$ vs *Pe*.

Brownian dynamics simulation with the surface bonding concept [31, 44, 45]. In this work, as in the previous studies, the maximum stress increased with *Pe* and the strain at maximum stress was insensitive to Peclet number (around $\gamma_{\max} = 0.15$). As *Pe* decreased, the stress overshoot gradually disappeared. The disappearance of stress overshoot could be correlated to the relaxation of flow-induced structural deformation by the thermal motion of the particles.

The gel point at which the liquid-to-solid transition begins is defined as a cross point of the storage modulus $\left(G'(\omega)\right)$ and the loss modulus $\left(G''(\omega)\right)$. At the gel point, the relaxation modulus can be shown to be [49]

$$G(t) = St^{-1/2}. \tag{3.2}$$

Therefore, the stress can be represented by

$$\begin{aligned} \sigma &= G(t)\gamma \\ &= St^{-1/2}\gamma. \end{aligned} \tag{3.3}$$

Considering that the strain at maximum stress $\left(\gamma_{\max}\right)$ was independent of shear rate, the time to reach the maximum stress $t_{\max}$ is given by

$$t_{\max} = \frac{\gamma_{\max}}{\dot{\gamma}}. \tag{3.4}$$

Using these relations, the maximum stress can be written in the form;

$$\begin{aligned} \sigma_{\max} &= St_{\max}{}^{-1/2}\gamma_{\max} \\ &= S\left(\frac{\gamma_{\max}}{\dot{\gamma}}\right)^{-1/2}\gamma_{\max} = S\gamma_{\max}{}^{1/2}\dot{\gamma}^{1/2} \end{aligned} \tag{3.5}$$

Based on this relation [45], we plotted the maximum stress against *Pe* on the log scale. From the plot (Figure. 3.1.4), we could confirm that the stress maximum and *Pe* has the relationship

$$\sigma_{\max} \propto Pe^{\alpha} \left(\alpha \approx 0.56\right) \tag{3.6}$$

which satisfies the theoretically derived power law behavior of Eq. (3.5) [45]. This power law behavior implies that the colloidal gel made in this simulation captures the important characteristics of the colloidal gel system effectively.

3.2. Structural change on the cluster length scale

Figure. 3.2.1 shows the snapshot of the particle configuration at each strain. The images were projected onto the flow (x) - shear gradient (y) plane at the center of the simulation box sliced with a thickness of $6a$. Different color implies different cluster with different size. Each particle has different color according to the size of the cluster to which the particle belongs. As more particles are aggregated, the particles belonging to that cluster become more reddish. At the initial state of strain zero, most of the particles were red. As the strain increased, the color of the particle changed from red to blue or green. This indicates that the colloidal gel ruptured and broke into small flocs or single particles under shear flow. Figure. 3.2.2 shows the size change of the largest cluster and the change of shear stress as a function of strain. According to the figure, we could divide the microstructural evolution into three regimes. In regime 1, the colloidal gel experienced deformation by imposed shear flow. Although some particles or small clusters were detached or even attached with small fluctuation of cluster size, the overall network was maintained without a remarkable structural change. In the meantime, the stress was accumulated in the networks of the colloidal gel during the deformation process. In regime 2, the colloidal gel began to rupture and the linear to non-linear transition of the stress occurred. In this rupture process, the stress decreased after passing the maximum and the largest cluster size decreased very rapidly with considerable fluctuation. The fluctuation implies that the structural evolution of the colloidal gel took place by the way of repeated aggregation and disaggregation rather than continuous disaggregation. After the rupture in regime 2, in regime 3, the stress reached steady state, while the largest cluster size reached steady state as well but with fairly large fluctuation.

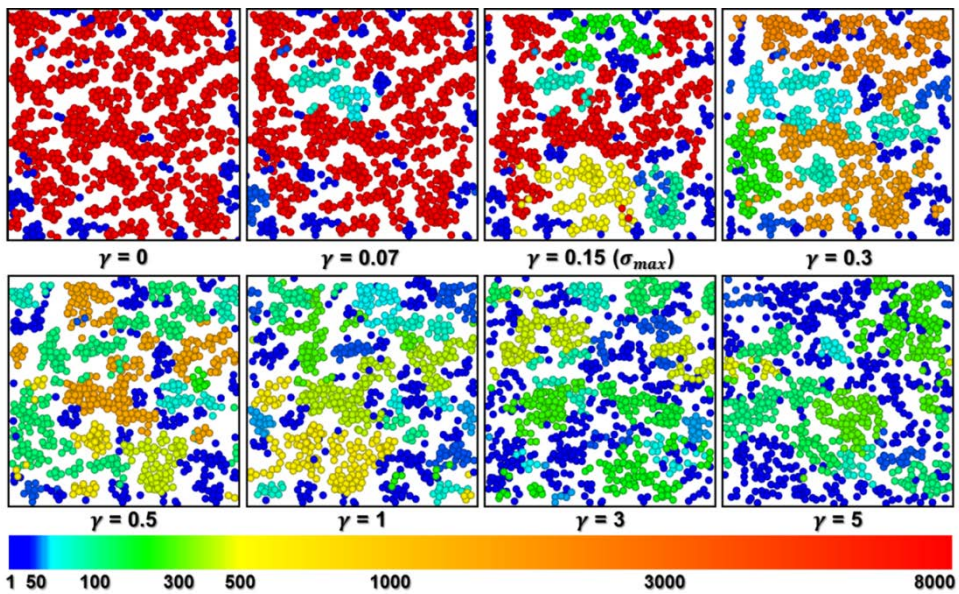

Figure. 3.2.1. Snapshot of the microstructure at different strain. The images were projected onto the flow-shear gradient(x-y) plane at the center of simulation box sliced with a thickness of 6*a*. The color implies the size of the cluster to which the particle belongs.

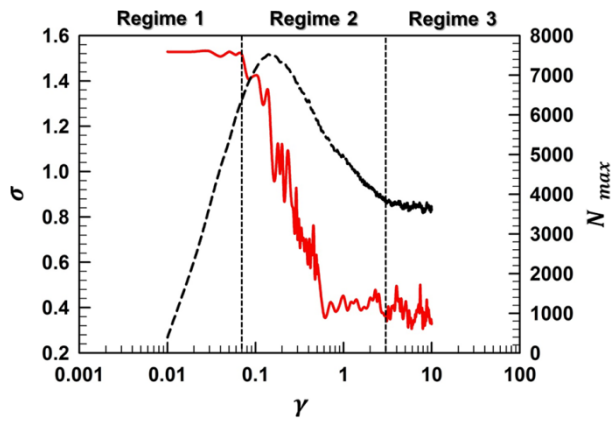

Figure. 3.2.2. Size change of the largest cluster(red solid line) and the change of shear stress(black dotted line) as a function of strain.

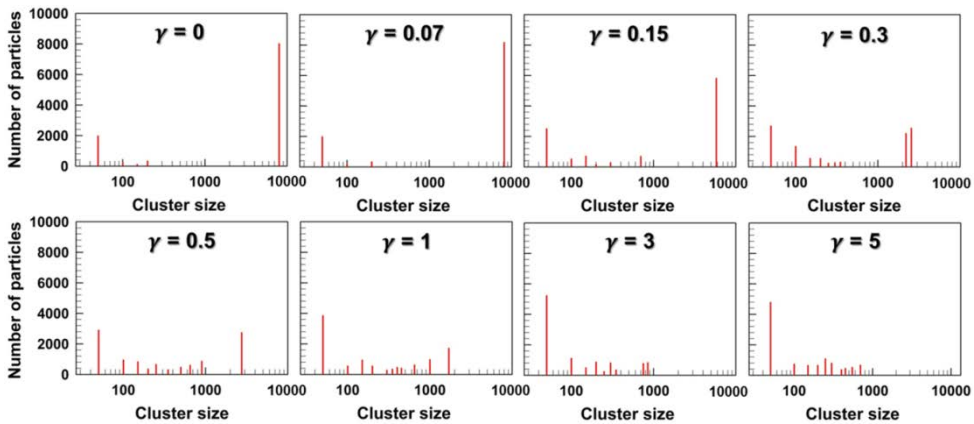

Figure. 3.2.3. Particle number distribution according to the cluster size at each strain.

An interesting event is the drastic decrease of the largest cluster size in regime 2. It clearly shows that the initial structural evolution of the colloidal gel is a kind of rupture process in which a percolated network structure is fractured into several large clusters. To see this more clearly, the particle number distribution according to the cluster size to which they belong was analyzed in Figure. 3.2.3. In each graph of the figure, x-axis represents the cluster size to which the particles belong and y-axis represents the number of particles (the product of cluster size and the number of clusters) belonging to each cluster size. Initially, in regime 1, a big peak around the cluster size 8000 and small peaks around cluster size 50 were observed. The big peak indicates that most of the particles belong to the percolated network structure and the small peaks indicate that only a small amount of the particles exist as small flocs. Because the gel deformed bearing stress in regime 1, the particle number distribution did not show any remarkable change, which corresponds to little change in the largest cluster size. But in regime 2, where the colloidal gel began to rupture, the big peak suddenly shrank and moved to the left. At the same time, several peaks appeared in the cluster size of hundreds to thousands. This change in particle number distribution represents that the percolated network structure of the colloidal gel ruptures into several large clusters of hundreds or thousands of particles in regime 2. As the strain increased, the peaks of large clusters were reduced in size and moved to the left. At the same time, the peaks of small flocs appeared and their number increased. This demonstrates the decomposition of the large clusters into many small flocs or single particles. In regime 3, where the stress and the largest cluster size reached steady state, no significant change in particle number distribution was observed.

Correlating the structural change on the cluster length scale to stress overshoot, a mismatch between the stress maximum and the initiation of the rupture was observed. In Figure. 3.2.2, entering into regime 2 at strain 0.07, the largest cluster size began to decrease dramatically. In Figure. 3.2.2, as strain increase from 0.07 (where the rupture started) to 0.15 (the stress maximum), the large peak which represents the percolated network structure of colloidal gel became smaller and

several small peaks appeared. In this strain range, even though the colloidal gel already started to rupture, the stress kept on increasing accompanied by linear to non-linear transition. It may look counter-intuitive that the initiation of the structural rupture did not directly lead to the stress decrease. However, from the linear to non-linear transition of stress observed in the strain range from 0.07 to 0.15, it is possible to explain the precedence of the structural rupture over the stress maximum as follows. In the strain range between 0.07 and 0.15, the stress increased with strain, despite the structural rupture which inevitably results in the stress decrease. In the colloidal gel, the stress increase can be attributed to the stress accumulation in the percolated network which bears the stress induced by the strain increase. Therefore, the stress increase by stress accumulation in the percolated network and the stress decrease by the structural rupture take place at the same time, and their competition decides whether the stress of the whole colloidal gel system increases or decreases. Right after the initiation of the rupture, most part of the colloidal gel maintains the network structure which can bear the stress induced by strain increase. However, as the strain increased further, the structural rupture proceeds and the stress decrease by the structural rupture gradually dominates over the stress increase by stress accumulation. The observed linear to non-linear transition which shows gradual slope change of the stress curve from positive to negative supports the competition between the stress decrease by the rupture of the colloidal gel and the stress increase induced by the strain increase. In this point of view, it would be reasonable to define the stress maximum as the balance of the competition.

3.3. Structural change on the local length scale

To get an idea on the topology change under shear flow, we calculated the bond number of the particles. Figure. 3.3.1 shows the average bond number change as a function of strain. The average bond number change could be divided into three regimes as in the analysis on the cluster length scale. Initially, the particles had an average bond number of 3.7, which means that each particle was connected to 3.7 of other particles. In regime 1, where only the deformation of the colloidal gel and stress accumulation was observed on the cluster length scale, the average bond number decreased very slightly. Entering into regime 2, where the rupture of the colloidal gel and the linear to non-linear transition started, the average bond number decreased significantly. The average bond number continuously decreased until regime 3. In regime 3 where the stress reached a steady state, the average bond number also reached a steady value of 2.3. In this simulation, the non-central forces induced by the bonds between the particle surfaces describe the rotational motion of the particle and restrict the angular reorganization. Thus, the higher bond number of the particle implies a lower chance of the angular reorganization and the particles with high bond number represent the rigid structure which can support the stress. On the other hand, the particles with low bond number experience relatively little restriction and easily relax from the distortion and they results in low elastic resistance. Therefore, the decrease of the average bond number from 3.7 to 2.3 implies a transition from the initial multiply-connected rigid chain to singly-connected soft chain. This character is also observed in Figure. 3.2.1, in which the structure at strain 5 shows more slender chains compared to the initial structure at strain 0. To understand the topology change more accurately, we looked into the bond number distribution change along with the strain increase. Figure. 3.3.2 shows the bond number distribution change at each strain, relative to the initial bond number distribution in Figure. 3.1.2. In Figure. 3.3.2, all the points at strain. 0.07 are located close to the probability change of zero, which means that the bond

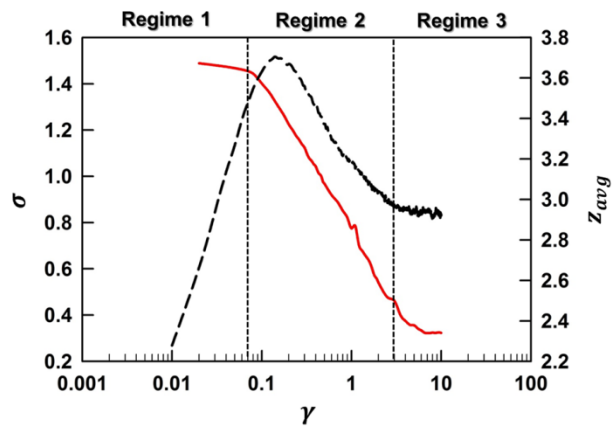

Figure. 3.3.1. Stress(black dotted line) and the average bond number(red solid line) change as a function of strain.

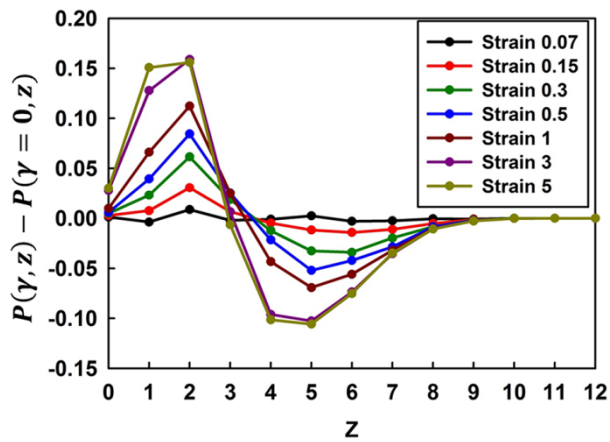

Figure. 3.3.2. Bond number distribution $\left(P\left(z,\gamma\right)\right)$ change relative to initial bond number distribution $\left(P\left(0,\gamma\right)\right)$ for non-central interaction model.

number distribution rarely changed in regime 1. As the strain increased to regime 2, the fraction of particles with bond number higher or equal to 4 decreased and the fraction of particles with bond number lower than 4 increased. This corresponds well with that of the preceding research, where highly significant correlation between the elasticity of the colloidal gel and the fraction of rigid clusters was found. The bond number distribution change which shows the change from high to low bond number verifies that the structural evolution of the colloidal gel under shear flow can be thought of as a transition of the multiply-connected rigid chains to singly-connected soft chains. Thus, on the local length scale, considering that the origin of the elasticity of the colloidal gel is the rigid chains [17, 53, 54], the linear to non-linear transition could be regarded as the topological change from the multiply-connected rigid chain to the singly-connected soft chain.

The structural analysis on the local length scale provides information on the criterion for cluster rigidity. In the preceding study [19], the rigidity of the particles was analyzed through the contact number of the particles which is equivalent to the bond number of this simulation. The particles with low contact number easily relax from their non-equilibrium state and cannot support stress. On the other hand, the particles with high contact number experience slow relaxation which makes it possible to support stress. Therefore, the high contact number is related to the rigidity of the particles. In the preceding study, the stress-bearing rigid particle was regarded as the particle with the contact number higher or equal to 6, which is the rigidity criterion of the particles interacting through central forces. However, not only the contact number 6 but also the contact number 4 was strongly correlated to the elasticity and the correlation between the contact number 4 and elasticity was expected to be associated with the influence of the non-central and tangential interaction between the particles. So, they suggested the contact number 4 as a lower limit of the rigidity criterion. In our work, where the non-central and tangential interactions of the particles were considered, the bond number distribution change corresponded with the contact number distribution change of the preceding study, showing the increase of the particles with bond number lower

than 4 and decrease of the particles with bond number higher than or equal to 4. Therefore, our simulation supports that the bond number (or contact number) of 4 is the proper lower limit of the rigidity criterion.

The correlation between the bond number and rigidity was also observed in the simulation of classical Brownian dynamics, in which only the central interaction between the particles were considered. To examine the influence of the non-central interaction, we compared the two models; one with non-central interaction and the other without non-central interaction. Figure. 3.3.3 shows the bond number distribution change without non-central interaction. As in the preceding research and non-central interaction model, the fraction of the particles with bond number lower than 4 increased and that of the particles with bond number higher than or equal to 4 decreased. However, the non-central interaction made a significant difference in bond number distribution change. Comparing the bond number distribution changes of non-central (Figure 3.3.2) and central models (Figure 3.3.3), the probability change of the central model is about twice larger than that of the non-central model. In the case of central interaction model, the multiply-connected rigid chains with high bond number more easily changed into soft chains with low bond number. This difference indicates that the non-central interaction between the particles plays a major role in determining the microstructural change. The non-central interaction also changed rheological properties. The inset in Figure. 3.3.3 shows the stress growth curves of two models. The stress curve of the non-central model shows steeper stress increase and much higher stress than that of the central model. These structural and rheological differences are attributed to the non-central interaction, and this enhances the rigidity which is closely related to the stress bearing microstructure.

In the preceding research about colloidal gel at low volume fraction [26,27,31,33], the ruptured clusters and the particles underwent shear induced densification which resulted in compactly packed structure with bond number increase. But in this study on the colloidal gel at intermediate volume fraction, such

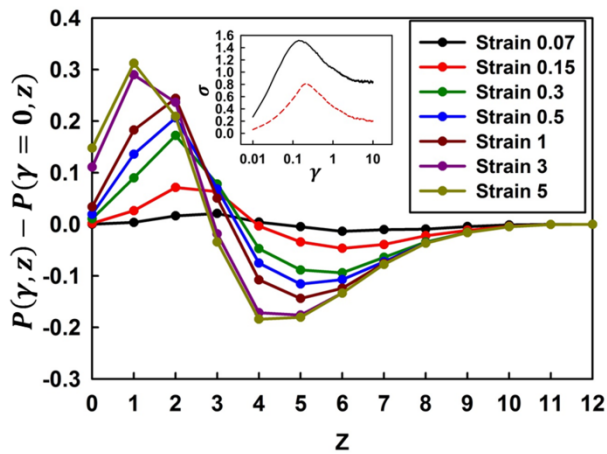

Figure. 3.3.3. Bond number distribution change $\left(P\left(z,\gamma\right)\right)$ relative to initial bond number distribution $\left(P\left(0,\gamma\right)\right)$ for central interaction model. Inset shows the stress growth curves of the non-central interaction (black solid line) and central interaction (red dotted line).

a shear-induced densification was not observed. The major reason for the absence of densification can be thought of as follows. First, the surface bonding concept used in this simulation can be one reason. With only central attractive interaction, the particles can move freely about other particle centers, resulting in structural reorganization to thermodynamically favored phase [51]. However, with the surface bonding, the particles lose their freedom to move about the centers of the other particles [45]. Thus, the surface bonding concept restricts the angular reorganization of the particles which is one of the major mechanisms of densification. The transition of multiply-connected rigid chains to singly-connected soft chains without densification is similar to the previous results [57, 58]. In the preceding research, by using the sticky particle model, which also restricts angular reorganization, no densification was observed and the clusters were disaggregated forming string-like linear chains, leading to the decrease of the bond number, which is in good agreement with this study [57]. Secondly, the effect of strong shear flow and weak particle interaction can be another reason. The bond number change was determined by the competition of shear-induced densification which increased the bond number and flow-induced changes in cluster size which decreased the bond number. Under shear flow, the clusters show diverse behaviors according to the conditions such as shear rate and particle interaction [23]. Different from the previous studies on the colloidal gel at low volume fraction, in this work, relatively stronger shear flow should be applied to rupture the colloidal gel at intermediate volume fraction. According to the theoretical modeling [59] under strong shear flow, the clusters break-up before densification takes place. As the attractive interactions between the particles become weaker, this tendency becomes clearer. Therefore, in this work with strong shear flow and weak interaction between the particles, flow-induced cluster size change overwhelmed the shear-induced densification, and the bond number decreased continuously until the steady state was achieved.

3.4. Structural anisotropy

Figure. 3.4.1 shows the projection of the pair distribution function in the shear-gradient (x-y) plane, which gives the structural information on the local length scale. The pair distribution projection was calculated for a slice of thickness a (particle radius) with the bin of size $\delta r = 0.01a$ and averaged for five different simulation sets with different random motion and initial configuration of the particles. Initially, at strain 0, the pair distribution function was isotropic. At strain 0.07 belonging to regime 1, where no remarkable structural change was observed, the pair distribution function did not show any significant change as in the structure analysis on the cluster length scale and the local length scale. Entering into regime 2, at strain 0.15, the pair distribution function began to exhibit break-up along the extensional direction. As the strain increased further from 0.3 to 0.5, strong break-up along the extensional axis occurred. Associating this with the structural analysis on both cluster length scale and local length scale, the change in pair distribution function was found to be related with the rupture of the percolated network to several large clusters. During this process, no significant change of pair distribution function occurred along the compressional axis. However, as the large clusters decomposed into many small flocs at higher strain, the pair distribution function along the compressional axis began to decrease. In the Figure. 3.4.1, the pair distribution function at strain 3 and 5 showed almost the same shape. From these results, we can verify that in regime 3 where the strain is higher than 3, the pair distribution function reached a steady state as was the case for other structure indices.

To analyze the structural anisotropy quantitatively, we measured the bonding angle between the particles for a slice of thickness a as was done for pair distribution function, and averaged bonding angles over all particles. As shown in Figure. 3.4.2, the bonding angle was defined as the angle between the flow

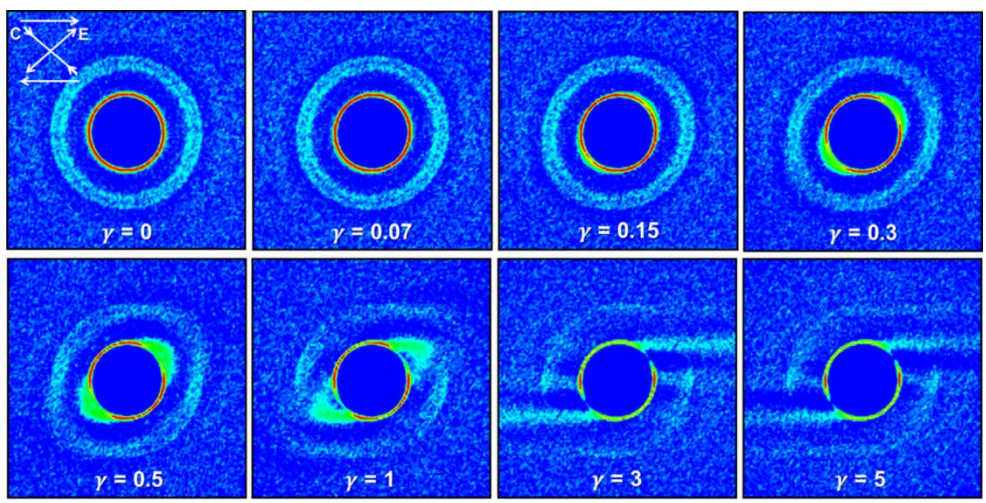

Figure. 3.4.1. Pair distribution function at different strains (projected onto the flow-shear gradient (x-y) plane)

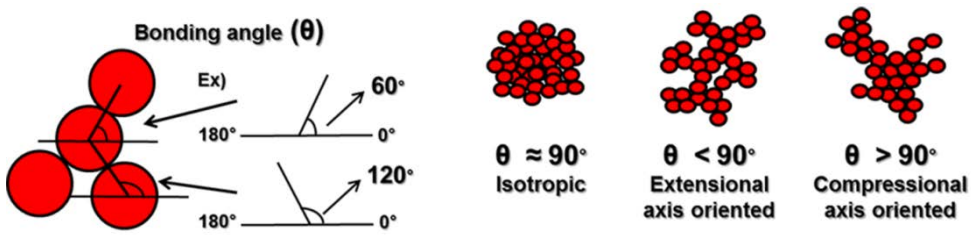

Figure. 3.4.2. Schematic for measurement of average bonding angle.

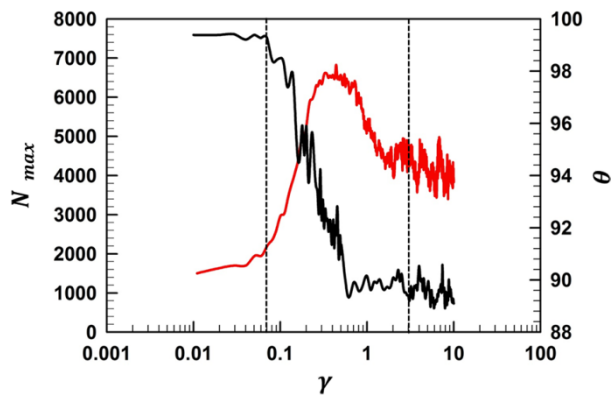

Figure. 3.4.3. Largest cluster size (black solid line) and average bonding angle (red solid line) as a function of strain.

direction (x-axis) and the line connecting the centers of two particles projected on the shear-gradient (x-y) plane. For an isotropic structure, the average bonding angle should be $90°$. But if a structure is oriented to the extensional direction or to the compressional direction, the average bonding angle will be below or above $90°$, respectively. Figure. 3.4.3 shows the average bonding angle together with the largest cluster size as a function of strain. Initially, the colloidal gel showed the average bonding angle of nearly $90°$, from which isotropic structure of the colloidal gel was verified. In regime 1, the average bonding angle increased very slightly. But, in regime 2, where the rupture and linear to non-linear transition started, the average bonding angle increased very rapidly. The average bonding angle increased continuously until it reached maximum, after which it decreased and reached a steady state in regime 3.

During the structural evolution, anisotropy was observed in the compressional axis direction showing the average bonding angle higher than $90°$. The structural anisotropy in the compressional axis direction is different from that of the colloidal gel at low volume fraction. In the previous study at low volume fraction, the structural anisotropy was induced in the extensional axis direction by the free rotation of singly-connected regions of the gel backbone [26, 27]. This disagreement indicates that the colloidal gel at intermediate volume fraction experiences a unique structural evolution different from that of the low volume fraction. In many experiments of colloidal suspensions, the structural anisotropy in the compressional axis direction has been observed, which is in good agreement with our simulation [24, 37]. This flow-induced anisotropy could be correlated with the experimentally observed three representative direction-dependent motions: interlocking, rotation and break-up. The direction-dependent behaviors were also observed in this study. Figure. 3.4.4 (a) shows the interlocking of two clusters along the compressional axis. Because this interlocking of aggregates increases the number of bonds along the compressional axis, it results in an increase of the average bonding angle. Figure. 3.4.4 (b) shows the rotational motion toward the

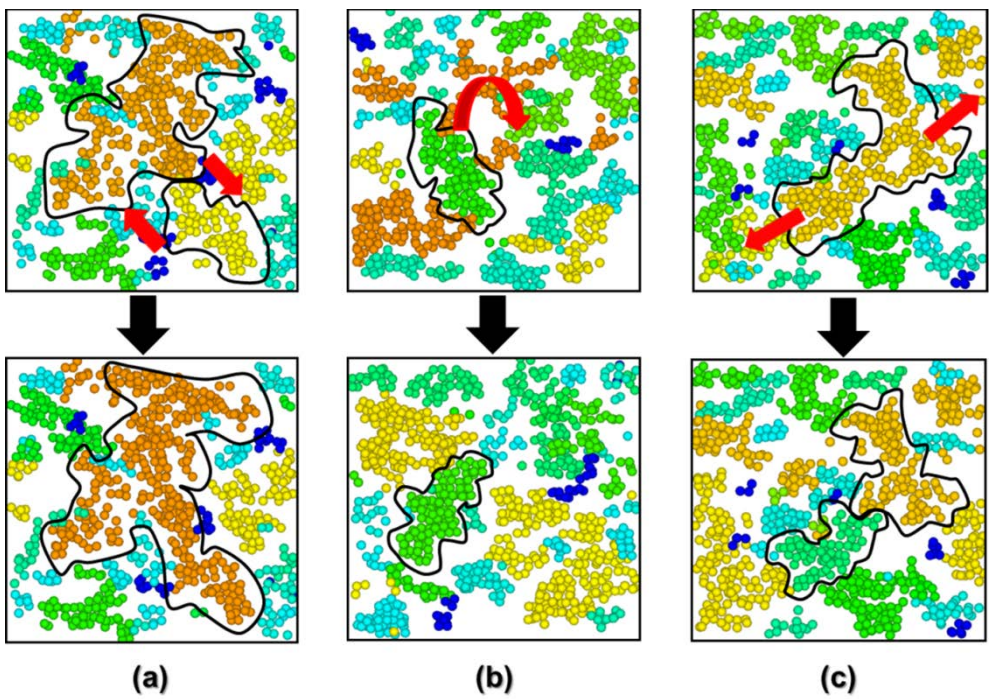

Figure. 3.4.4. Three representative motions of clusters observed in the flow-shear gradient (x-y) plane with a thickness of 6*a*: (a) interlocking along the compressional axis, (b) rotation toward the flow direction, (c) break-up along the extensional axis (clusters with less than 20 particles were erased for clarity).

flow direction. Rotational motion makes clusters tilt toward the flow direction (here, clockwise)and as a result, the average bonding angle decreases. Figure. 3.4.4 (c) shows the break-up behavior along the extensional axis. In this process, the number of bonds in the extensional axis direction decreases, which leads to the increase in the average bonding angle.

Associating the average bonding angle change (Figure. 3.4.3) with the direction-dependent cluster behaviors (Figure. 3.4.4), which are observed in this simulation as well as in experiments, the structural evolution mechanism of the colloidal gel could be drawn. At first, when the shear flow is imposed, the colloidal gel is deformed by shear flow but no remarkable structural change occurs. The average bonding does not show meaningful change either. At the early stage of the rupture, the average bonding angle increases rapidly. The increase of the average bonding angle can be associated with the break-up along the extensional axis. The pair distribution function change along the extensional axis which appears in Figure. 3.4.1 supports this argument. The average bonding angle decrease after the maximum point can be correlated with the rotational motion of the clusters. Initially, the particles are aggregated in the form of percolated network structure. In this structure, the rotational motion of the clusters is hard to take place as it is hindered by the presence of network branches. But as the percolated network structure is fractured into separate clusters, the rotational motion towards the flow direction becomes easier. Actually, the average bonding angle started to decrease as the largest cluster size reached the steady value, as shown in Figure. 3.4.3. As the clusters are tilted from the compressional axis direction to the extensional axis direction by the rotational motion, the average bonding angle decreases. Repeating the rotation and break-up, the clusters are decomposed into small flocs. Finally the average bonding angle reaches a steady state with some fluctuation. In regime 3, where other structure indices reached steady state, the decomposed small flocs continuously undergo interlocking along the compressional axis, rotation toward the flow direction and break-up along the extensional axis, and finally results in an average bonding angle of steady value with some fluctuation.

Chapter 4. Structural anisotropy and rheological behavior of colloidal gel under start-up shear flow

4.1. Simulation system

Figure. 4.1.1 presents rheological and structural information on the model colloidal gel system. Figure. 4.1.1 (A) demonstrates initial gel structure at quiescent state. Initially, 99% of the total particles were aggregated to compose a percolated network structure. Under shear flow, the colloidal gel experiences various structural changes. The angular averaged pair distribution function $\langle g(r,\theta,\varphi)\rangle_{\theta,\varphi}$ in Figure. 4.1.1 (B), which can be considered as radial distribution, demonstrates the structural changes. Under shear flow, as strain increases to reach steady state, $\langle g(r,\theta,\varphi)\rangle_{\theta,\varphi}$ shows decrease in the first maximum peak. Considering that the first maximum peak, which is called as nearest neighbor peak, corresponds to particle length scale local structure, the angular averaged pair distribution function change under shear flow can be recognized as a result of shear-induced local structural change. The shear-induced structural change is also expressed as decrease in second maximum peak, which is called the second nearest neighbor peak.

The structural change manifests itself as non-linear rheological behavior. In Figure. 4.1.1 (C), the stress growth under start-up shear is shown as a function of strain. As strain increases, the stress increases up to a maximum stress and then the stress decreases to a steady value. The maximum stress increases with Pe and the strain at maximum stress is invariable. This stress-overshoot behavior has been studied in terms of structural rupture of colloidal gel [20], which is represented by decrease in the maximum peaks of $\langle g(r,\theta,\varphi)\rangle_{\theta,\varphi}$ in this work. In the beginning of start-up shear, the colloidal gel experiences deformation, maintaining the network structure. During this deformation, the stress is accumulated in the network structure showing linear rheological behavior. However, as strain increases further, the stress-bearing network structure is ruptured and the colloidal gel shows decrease in stress.

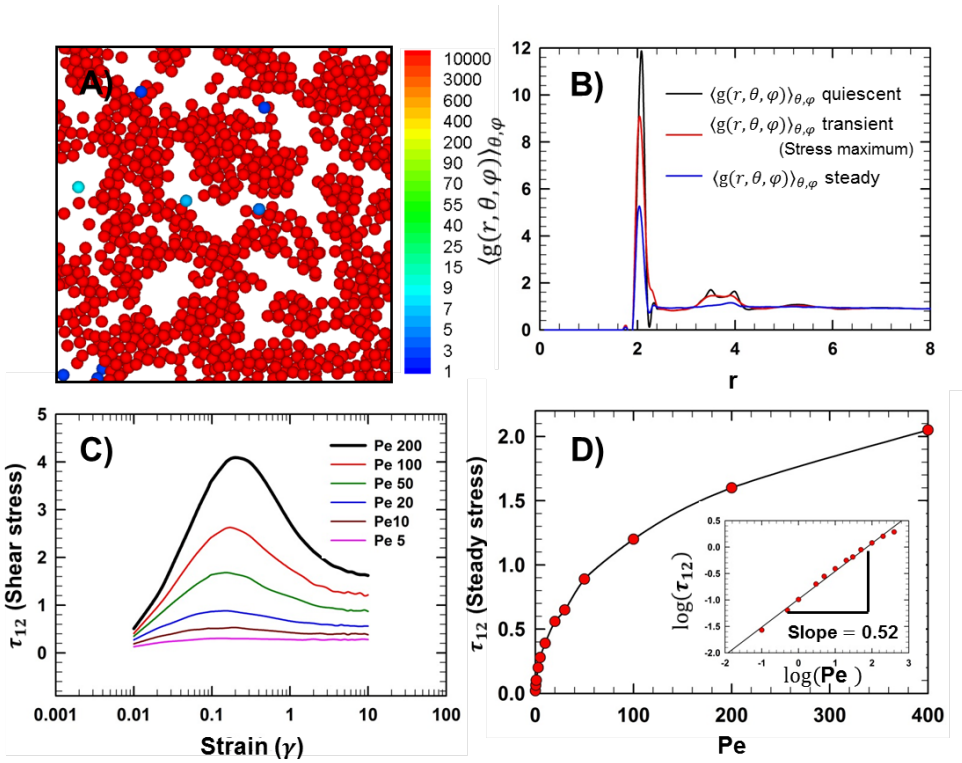

Figure. 4.1.1. (A) Gel structure (20% volume) at quiescent state. The image shows particles at the center of the simulation box sliced with a thickness of 4a. The color indicates the size of cluster to which the particles belong. **(B)** Angular averaged pair distribution function $\langle \mathbf{g}(\mathbf{r},\boldsymbol{\theta},\boldsymbol{\varphi})\rangle_{\boldsymbol{\theta},\boldsymbol{\varphi}}$ (radial distribution function) of the colloidal gel in a quiescent state, transient state, and steady state under steady shear flow of Pe 200. **(C)** Stress-overshoot behavior of the colloidal gel. In this work, Pe 200 case (thick black curve) is mainly studied. **(D)** Flow curve of the colloidal gel. Inset shows the result on a log scale.

In Figure. 4.1.1 (D), steady shear measurements demonstrate the shear thinning behavior of the colloidal gel. At low Pe, where the particles are easily relaxed from shear-induced deformation, the colloidal gel maintains its structure showing relatively high viscosity. However, as Pe is increased, shear force has an influence on the colloidal gel structure. Shear force hinders the relaxation of the colloidal gel structure and induces rupture of the colloidal gel structure, which leads to decrease of the viscosity. The inset in Figure. 4.1.1 (D) shows the flow curve on a log scale. The steady shear stress and Pe demonstrate power-law behavior with exponent 0.52. This result is in agreement with the prediction of the soft glassy material rheology (SGR) model [60, 61, 62], which has been employed to study soft materials, such as colloidal glasses and colloidal gel.

4.2. Structural anisotropy under start-up shear

It has been shown that the colloidal gel experiences structural change under startup shear flow accompanied with nonlinear rheological behavior. In this section, to study the structural change in respect of structural anisotropy, the colloidal gel structure was analyzed through the pair distribution function and the structure factor. Figure. 4.2.1 shows the diagrams of the structural anisotropy analysis. Based on the particle configuration, the pair distribution function and the structure factor were calculated in three orthogonal planes of velocity-gradient, velocity-vorticity and gradient-vorticity. By investigating the pair distribution function change and the structure factor change in the transient state between the quiescent state and the steady state, the development of the structural anisotropy of the colloidal gel under startup shear has been analyzed and correlated to the relevant stress responses.

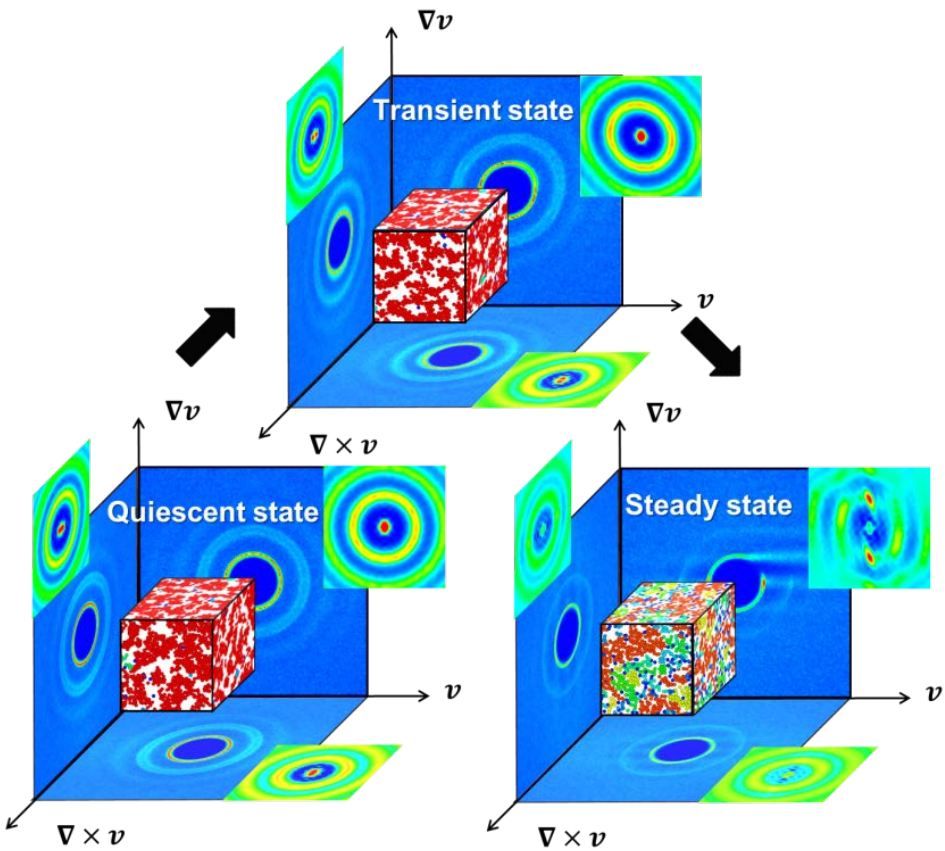

Figure. 4.2.1. Diagrams of colloidal gel structure analysis. The simulated colloidal gel configurations are analyzed through pair distribution function (large plane with bluish color) and structure factor (small plane with greenish color). The pair distribution function and structure factor are calculated in the three perpendicular planes of velocity-gradient $(\mathbf{v} - \boldsymbol{\nabla}\mathbf{v})$, velocity-vorticity $(\mathbf{v} - \boldsymbol{\nabla} \times \mathbf{v})$, and gradient-vorticity $(\boldsymbol{\nabla}\mathbf{v} - \boldsymbol{\nabla} \times \mathbf{v})$.

4.2.1. Structural anisotropy in the velocity-gradient plane

Top row in the Figure. 4.2.2 shows the pair distribution function difference Δg in velocity($\boldsymbol{v}$)–gradient($\boldsymbol{\nabla v}$) plane during the startup shear. As strain increases, innermost ring of the pair distribution function difference, which corresponds to nearest neighbor structure, shows strong decrease along the extensional axis of shear. In contrast, along the compressional axis of shear, relatively slight pair distribution function change is observed. This pair distribution function change indicates the structural anisotropy along the compressional axis. The structure factor shows the structural anisotropy along the compressional axis as well. In the middle row of Figure. 4.2.2, structure factor difference ΔS in velocity$(\boldsymbol{v})$–gradient$(\boldsymbol{\nabla v})$ plane is demonstrated. Between the black circles, which delineate q range corresponding to the nearest neighbor structure, the structure factor shows increase along the extensional axis and decrease along the compressional axis. Considering the inherent inverse relationship between reciprocal space and real space, the structure factor, which analyzes the microstructure in reciprocal space, shows patterns that corresponds to 90˚ rotation of the pair distribution function. Therefore, the increase in the structure factor along the extensional axis can be correlated to the compressional axis direction oriented microstructure in real space.

The structural anisotropy can be analyzed quantitatively by investigating angular variation of the pair distribution function and the structure factor over the entire contact surface ($r = 2$ and $q = q^*$). Figure. 4.2.3 shows the angular variation of the pair distribution function $g(2, \theta_{12})$ and the structure factor $S(q^*, \varphi_{12} + 90°)$. Here, the abscissa of the structure factor is given as a function of $\varphi_{12} + 90°$ to consider the inverse relationship between reciprocal space and real space. (The

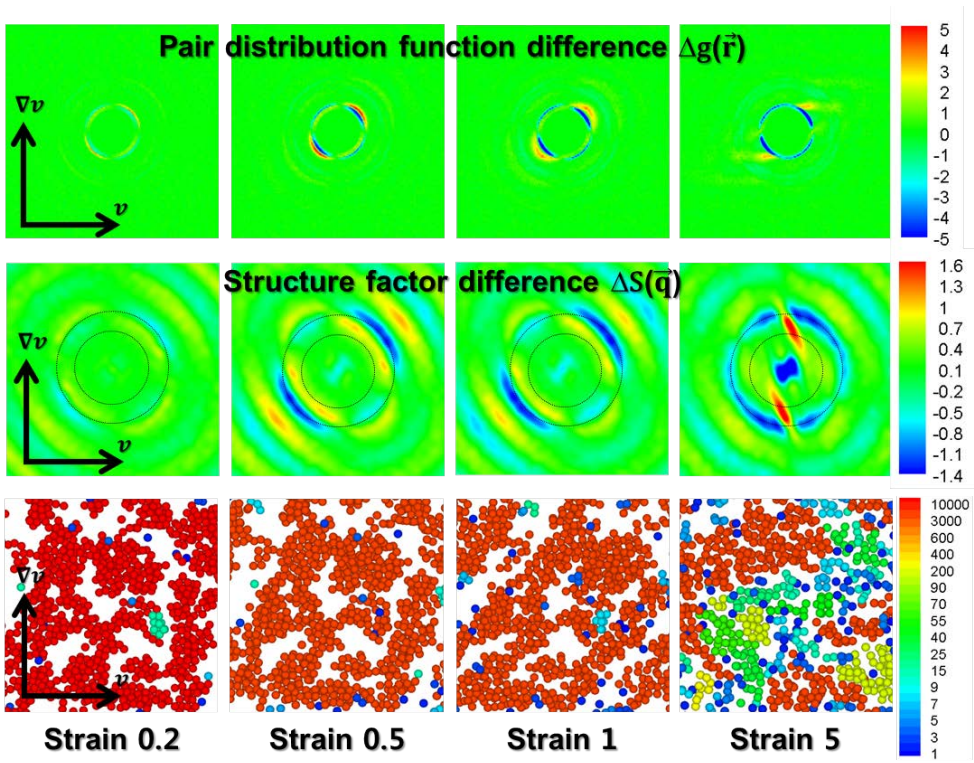

Figure. 4.2.2 Pair distribution function difference $\left(\Delta\mathbf{g}(\vec{\mathbf{r}},\boldsymbol{\gamma}) = \mathbf{g}(\vec{\mathbf{r}},\boldsymbol{\gamma}) - \mathbf{g}(\vec{\mathbf{r}},\boldsymbol{\gamma}=\mathbf{0})\right)$ (top row) and structure factor difference $\left(\Delta\mathbf{S}(\vec{\mathbf{q}},\boldsymbol{\gamma}) = \mathbf{S}(\vec{\mathbf{q}},\boldsymbol{\gamma}) - \mathbf{S}(\vec{\mathbf{q}},\boldsymbol{\gamma}=\mathbf{0})\right)$ (middle row) in the velocity($\boldsymbol{v}$)–gradient($\boldsymbol{\nabla v}$) plane. Snapshots of the particle configuration (bottom row). The images show the particles in the velocity-gradient plane sliced with a thickness of 4a. The color indicates the size of the cluster to which the particles belong. The black circles in the structure factor difference indicate the *q* range ($\boldsymbol{q}^*$) corresponding to the nearest neighbor structure.

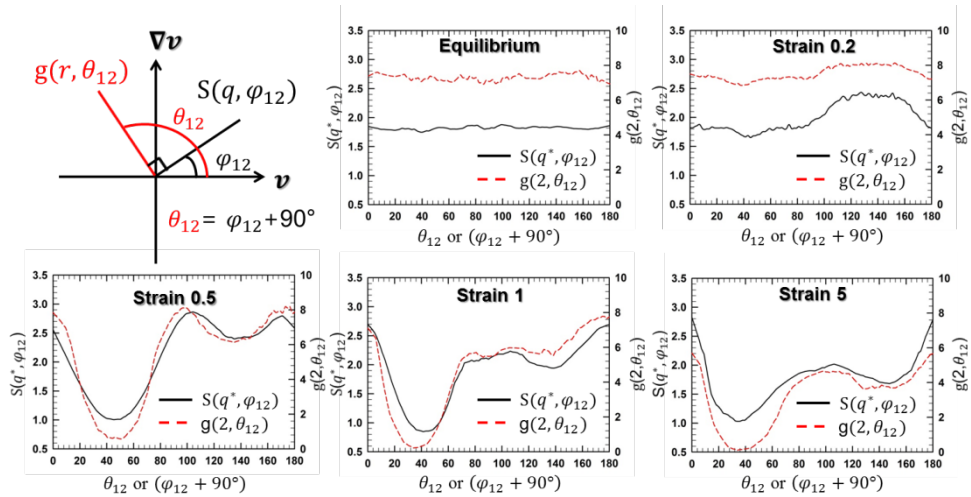

Figure. 4.2.3. Angular variation of the pair distribution function ($g(r, \theta_{12})$) and the structure factor $S(q, \varphi_{12} + 90°)$ over the entire contact surface ($r = 2,\ q = q^*$) in the velocity($\boldsymbol{v}$)-gradient($\boldsymbol{\nabla v}$) plane.

angular variation analysis in the velocity($\boldsymbol{v}$)–vorticity($\boldsymbol{\nabla \times v}$) plane and gradient ($\boldsymbol{\nabla v}$)–vorticity ($\boldsymbol{\nabla \times v}$) plane will employ the same notation.) At equilibrium state of strain 0, both the pair distribution function and the structure factor demonstrate isotropic structure, which is described by flat curves. The strain increase from strain 0 to strain 0.2 induces the pair distribution function change and the structure factor change. The angular variation at strain 0.2 shows increase in the pair distribution function and the structure factor along the compressional axis direction ($\theta_{12} = \varphi_{12} + 90° = 135°$). On the other hand, no remarkable change is observed in the extensional axis direction ($\theta_{12} = \varphi_{12} + 90° = 45°$). As strain increases to strain 0.5, rapid decrease in the pair distribution function and the structure factor is observed in the extensional axis direction. On the other hand, the pair distribution function and the structure factor in the compressional axis rarely change. As strain increases further and reaches steady state (strain 5), the colloidal gel shows overall decrease in the pair distribution function and the structure factor. Nevertheless, the pair distribution function and the structure factor show strong anisotropy along the compressional axis. The structural anisotropy change can be correlated to the structural evolution mechanism of colloidal gels under startup shear [20]. Initially, when shear flow is imposed, the colloidal gel is deformed by shear flow. The slight increase in the pair distribution function and the structure factor along the compressional axis direction at strain 0.2 indicates that the initial structural change of the colloidal gel takes the form of compression. As strain increases more, the colloidal gel structure undergoes break-up along the extensional axis. The break-up, which prefers the extensional direction, induces depletion of neighboring particles along the extensional axis, while the microstructure along the compressional axis is maintained (strain 0.5). As strain increased further, the colloidal gel network structure undergoes rotational motion toward the flow direction and ruptured into several clusters and flocs as shown in Figure. 4.2.2 (strain 5). The rotation and breakup of the overall colloidal gel structure bring about the overall decrease in the pair distribution function and the structure factor. In this process, despite the overall decrease of the pair distribution function and the structure factor, the

breakup along the extensional axis and the shear-induced aggregation along the compressional axis still cause structural anisotropy along the compressional axis.

At steady state (strain 5), where the colloidal gel is ruptured into several clusters and flocs, the colloidal gel shows the structural anisotropy, which is similar to that of the hard sphere system. In addition to the structural anisotropy along the compressional axis, the ruptured colloidal gel shows the string-like organization along the flow direction, which is represented by the increase of the structure factor along the gradient axis in Figure. 4.2.2 (strain 5). The alignment along the flow direction has been observed in previous theoretical [63, 64] and experimental works with hard sphere system [65,66]. Besides the alignment along the flow direction, the overall angular distribution of the ruptured colloidal gel in Figure. 4.2.3 (strain 5) shows similarity to the hard sphere system.

Analysis through spherical harmonics expansion of the pair distribution function $g(\vec{\mathbf{r}})$ gives information on the structural anisotropy in detail. In the Figure. 4.2.4 (A), spherical harmonic coefficient $g_2^2(r)$ at each strain, which denotes the intensity of spherical harmonic term X_2^2, is displayed. Initially, at strain 0, $g_2^2(r)$ is described by a flat curve, which corresponds with the isotropic colloidal gel structure at equilibrium state. As strain increases, the result shows two peaks at $r \cong 2$ and in between 2 and 2.15. At $r \cong 2$, the peak shows minima of negative value. Because X_2^2 describes an anisotropic structure along the extensional axis as shown in the inset of the Figure. 4.2.2 (A), the negative value of $g_2^2(r)$ can be interpreted as a result of anisotropic structure along the compressional direction. On the other hand, in between 2 and 2.15, $g_2^2(r)$ demonstrates maxima with positive value, which indicates an anisotropic structure along the extensional axis. The different structural anisotropies at different r are associated with the particle motion under shear flow. Under shear flow, particles approach to each other along the compressional axis. At the same time, particles are convected away along the extensional axis. Therefore, at $r \cong 2$, where particle surfaces bump into each other, the colloidal gel shows structural anisotropy along

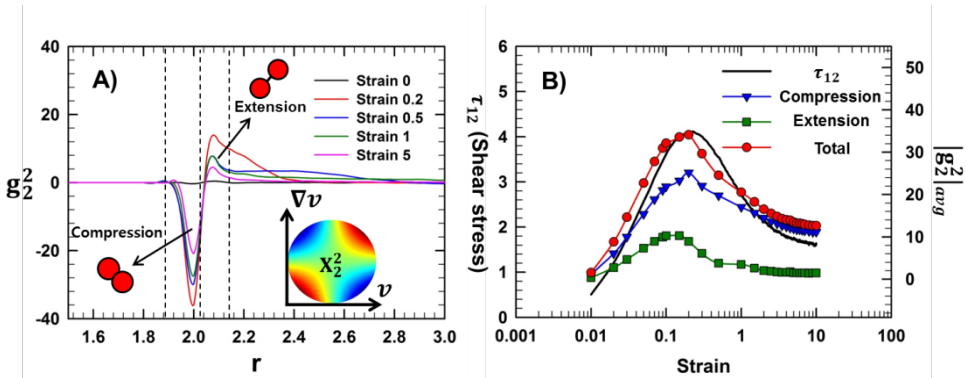

Figure. 4.2.4. A) Spherical harmonic function $\boldsymbol{X_2^2}$ (inset) and coefficient $\mathbf{g_2^2}$. Dotted lines denote the compression part and the extension part. **B)** Absolute value of $\mathbf{g_2^2}$ coefficient averaged over compressional part (blue down triangle) and extensional part (green square) and sum (red circle) as a function of strain ($\boldsymbol{\gamma}$). Black solid line shows shear stress response $\boldsymbol{\tau_{12}}$ of the colloidal gel.

the compressional axis with negative $g_2^2(r)$. On the other hand, in between 2 and 2.15, the structural anisotropy along the extensional axis is observed, because the particle bonds are stretched to a value in between 2 (particle surface contact) and 2.15 (maximum stretching) by shear flow. As strain increases, decreased peaks are observed, which is ascribed to the rupture of the colloidal gel structure.

The structural anisotropy in velocity($\boldsymbol{v}$)-gradient($\boldsymbol{\nabla v}$) plane shows close correlation to the shear stress responses. In previous work [67], it has been shown that the shear stress τ_{12} can be given as

$$\tau_{12} = -\frac{2}{15}\pi\rho^2 \int_0^\infty r^3 g_2^2 \left(\frac{d\phi}{dr}\right) dr \tag{4.1}$$

where ρ is the particle number density and $\left(\frac{d\phi}{dr}\right)$ is the derivative of inter-particle potential, which is equivalent to inter-particle force. Even though Eq. (4.1) provides quantitative relationship between g_2^2 and the shear stress τ_{12}, this is not applicable to our work, where the inter-particle potential is given by a function of the bond length between the particle surfaces (b) as well as the inter-particle distance (r). Therefore, as a second string, we compared g_2^2 coefficient to the shear stress τ_{12}. To compare g_2^2 to τ_{12}, g_2^2 was averaged in compressional part and extensional part, separately. Because both of compressional part (negative g_2^2 and positive $\left(\frac{d\phi}{dr}\right)$ due to repulsive force by surface potential) and extensional part (positive g_2^2 and negative $\left(\frac{d\phi}{dr}\right)$ due to attractive force by bonding potential) contribute positively to τ_{12}, we compared the sum of $\left|g_2^2\right|_{avg}$ in the compressional part and extensional part to τ_{12}. Figure. 4.2.4 (B) shows the evolution of $\left|g_2^2\right|_{avg}$ and shear stress τ_{12} as a function of strain (γ). In addition to the stress overshoot behavior, $\left|g_2^2\right|_{avg}$ of the compressional part, the extensional part, and sum of them show overshoot behaviors. The overshoot behavior of the sum of the $\left|g_2^2\right|_{avg}$ corresponds with that of the stress curve, indicating the coincidence of the maxima of the $\left|g_2^2\right|_{avg}$ and τ_{12}.

4.2.2. Structural anisotropy in the velocity-vorticity plane

The top row of Figure. 4.2.5 shows the Pair distribution function difference Δg in the velocity ($\boldsymbol{v}$)–vorticity ($\boldsymbol{\nabla} \times \boldsymbol{v}$) plane under the startup shear. As strain increases, the innermost ring of the pair distribution function shows strong decrease along the velocity direction. On the other hand, compared with the change in the velocity direction, the innermost ring shows relatively slight decrease along the vorticity direction. The pair distribution function difference indicates the structural anisotropy along the vorticity axis. The structural anisotropy along the vorticity axis is also observed in the structure factor difference ΔS in the middle row of Figure. 4.2.5. As strain increases, the structure factor difference shows the intensity increases along the velocity axis, which is represented by the butterfly pattern. The butterfly pattern has been observed in many experimental works using scattering method [33, 35, 36]. In respect that the structure factor analyzes the microstructure in the reciprocal space, which has inverse relationship with real space, the butterfly pattern is an indication of a preferential alignment of particles along the vorticity direction.

The particle alignment along the vorticity axis has been observed in earlier work on hard sphere colloidal suspensions as well [65]. In case of hard sphere colloidal suspensions, the structural anisotropy along the vorticity has been considered to be induced by the hydrodynamic interactions between particles [38]. However, in our study, where the hydrodynamic interaction between particles is ignored, the structural anisotropy along the vorticity direction cannot be ascribed to the hydrodynamic interaction. The quantitative analysis through the angular variation of the pair distribution function $g(2, \theta_{13})$ and the structure factor $S(q^*, \varphi_{13} + 90°)$ in Figure. 4.2.6 suggests an explanation for how colloidal gel creates anisotropic structure along the vorticity direction. At equilibrium state of strain 0, as in the velocity($\boldsymbol{v}$)-gradient($\boldsymbol{\nabla v}$) plane, both the pair distribution function and

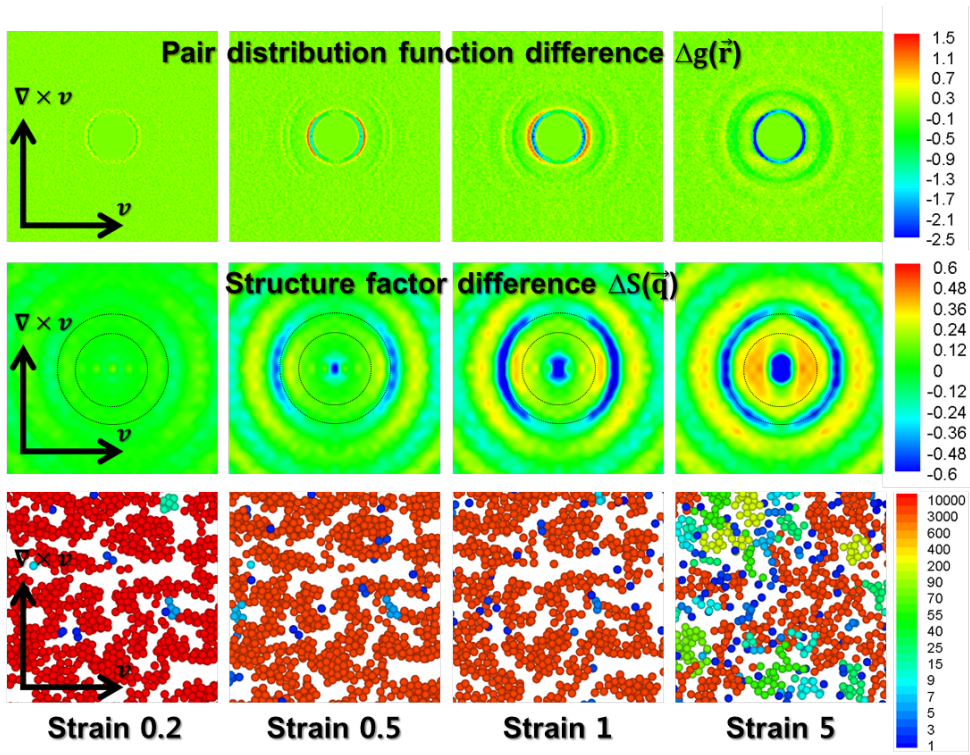

Figure. 4.2.5. Pair distribution function difference $\left(\Delta g(\vec{\mathbf{r}}, \gamma) = g(\vec{\mathbf{r}}, \gamma) - g(\vec{\mathbf{r}}, \gamma = 0)\right)$ (top row) and Structure factor difference $\left(\Delta S(\vec{\mathbf{q}}, \gamma) = S(\vec{\mathbf{q}}, \gamma) - S(\vec{\mathbf{q}}, \gamma = 0)\right)$ (middle row) in the velocity $(\boldsymbol{v})$ –vorticity $(\boldsymbol{\nabla \times v})$ plane. Snapshots of the particle configuration (bottom row). The images show the particles in the velocity $(\boldsymbol{v})$–vorticity $(\boldsymbol{\nabla \times v})$ plane sliced with a thickness of 4a. The color indicates the size of the cluster to which the particles belong. The black circles in the structure factor difference indicate the regime corresponding to the nearest neighbor structure.

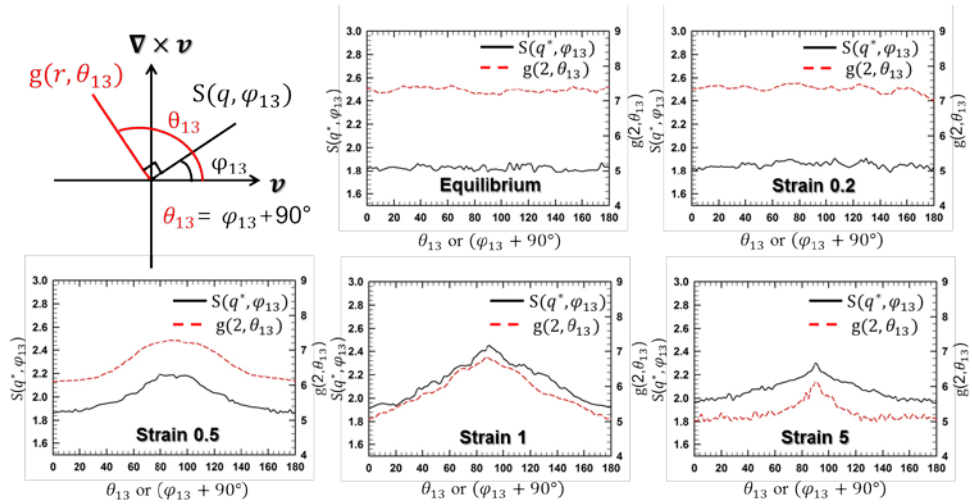

Figure. 4.2.6. Angular variation of pair distribution function $(\mathbf{g(2, \theta_{13})})$ and structure factor $\mathbf{S(q^*, \varphi_{13} + 90°)}$ in velocity$(\boldsymbol{v})$-vorticity$(\boldsymbol{\nabla \times v})$ plane.

the structure factor show isotropic structure, which is represented by flat curves. At strain 0.2, the pair distribution function and the structure factor rarely change and still show isotropic structure. Initially, the imposed shear flow induces no structural anisotropy along the vorticity direction. However, as strain increases further, the colloidal gel shows structural anisotropy along the vorticity axis. At strain 0.5, near the velocity axis ($\theta_{13} = \varphi_{13} + 90° = 0°$ or $180°$), the pair distribution function and structure factor decrease. Whereas, near the vorticity axis ($\theta_{13} = \varphi_{13} + 90° = 90°$), the pair distribution function maintains its initial value at strain 0 and some increase in structure factor is observed. This result explains the cause of the structural anisotropy along the vorticity axis. The shear flow can be considered as a linear combination of rotation field and extension field, which consists of the velocity direction component and the gradient direction component. The shear flow competes with the attractive inter-particle force to induce various forms of microstructural changes, a typical example of which is the structural rupture along the extensional axis shown in the result of velocity($\boldsymbol{v}$)-gradient($\boldsymbol{\nabla v}$) plane. The rupture in the velocity($\boldsymbol{v}$)-gradient($\boldsymbol{\nabla v}$) plane makes the colloidal gel experience microstructural change along the velocity direction ($\boldsymbol{v}$) and the gradient direction($\boldsymbol{\nabla v}$), which can be linked to the decrease of the pair distribution function and structure factor near the velocity axis. In contrast, there being no vorticity direction component in the shear flow, only attractive inter-particle force acts on the network structure along the vorticity direction. Therefore, the network structure in the vorticity direction undergoes relatively less microstructural change and maintains its structure longer, which leads to the higher value of the pair distribution function and the structure factor near the vorticity axis.

As strain increases more, at strain 1, the structural anisotropy along the vorticity axis gets more intensified. Near the vorticity axis, where the colloidal gel has a low probability of rupture, the colloidal gel maintains its structure and only slight decrease in the pair distribution function is observed. On the other hand, near the velocity axis, where the colloidal gel has a high probability of rupture, rapid decrease in the pair distribution function is observed. Therefore, the pair

distribution function and the structure factor show the intensified structural anisotropy, which is represented by a steep hill. As strain increases further, shear flow breaks the overall gel structure, even in the vorticity axis direction. Therefore, at strain 5, the pair distribution function demonstrates decrease in all direction including the vorticity axis. However, the colloidal gel still shows structural anisotropy along the vorticity axis, even though it is weakened.

The anisotropic structure in the velocity($\boldsymbol{v}$)- vorticity($\boldsymbol{\nabla \times v}$) plane can be linked to a linear combination of spherical harmonic terms, $2X_0^2 - X_1^2$, which is shown in the inset of Figure. 4.2.7 (A). In Figure. 4.2.7 (A), a linear combination of spherical harmonic coefficients, $2\mathrm{g}_0^2 - \mathrm{g}_1^2$, which is related to the intensity of $2X_0^2 - X_1^2$, is exhibited. Initially, at strain 0, $2\mathrm{g}_0^2 - \mathrm{g}_1^2$ shows flat curve because of the isotropic structure. As strain increases, two peaks are observed at $r \cong 1.95$ and in between 2 and 2.15. At $r \cong 1.95$, the peak shows minima of negative value and in between 2 and 2.15, the peak shows maxima with positive value. Considering that $2X_0^2 - X_1^2$ describes anisotropic structure along the vorticity axis, as shown in the inset of the Figure. 4.2.7 (A), the positive and negative value of $2\mathrm{g}_0^2 - \mathrm{g}_1^2$ indicate the anisotropic structure along the vorticity axis and velocity axis, respectively. Therefore, the small negative peaks at $r \cong 1.95$ can be interpreted as a weak structural anisotropy in the velocity direction. On the other hand, the large positive peaks in in between 2 and 2.15 can be associated with the anisotropic structure along the vorticity direction. As in the velocity ($\boldsymbol{v}$)-gradient ($\boldsymbol{\nabla v}$) plane, where the structural anisotropy exhibits close correlation to the shear stress τ_{12}, the structural anisotropy in the velocity ($\boldsymbol{v}$)-vorticity ($\boldsymbol{\nabla \times v}$) plane is also closely correlated to the rheological response, especially, the difference between τ_{11} and τ_{33}. The relationship between $2\mathrm{g}_0^2 - \mathrm{g}_1^2$, which describes the degree of the structural anisotropy in the velocity(v)-vorticity($\nabla \times v$) plane, and the normal stress difference $\tau_{11} - \tau_{33}$ is given as [67]

$$\tau_{11} - \tau_{33} = \frac{2}{15}\pi\rho^2 \int_0^\infty r^3(2\mathrm{g}_0^2 - \mathrm{g}_1^2)\left(\frac{d\phi}{dr}\right)dr. \quad (4.2)$$

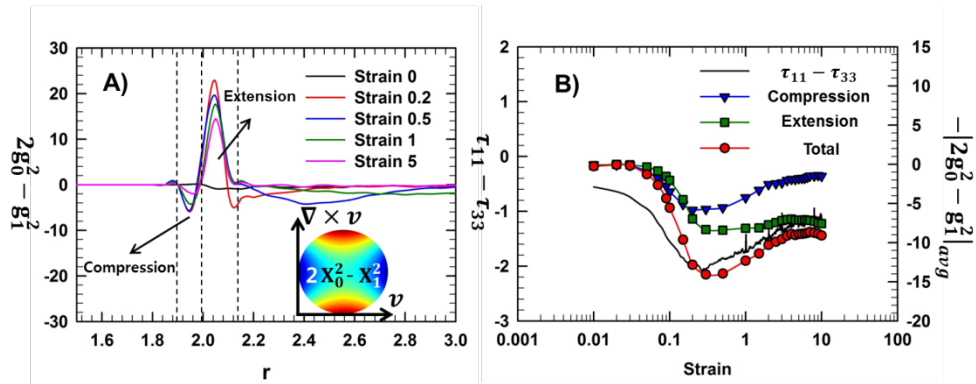

Figure. 4.2.7. A) A combination of spherical harmonic functions $\mathbf{2X_0^2 - X_1^2}$ (Inset) and coefficients $\mathbf{2g_0^2 - g_1^2}$, which correspond to the structural anisotropy along vorticity direction in the velocity($\boldsymbol{v}$)- vorticity($\boldsymbol{\nabla \times v}$) plane. Dotted lines denote the compression part and the extension part. **B)** Absolute value of $\mathbf{2g_0^2 - g_1^2}$ averaged over compressional part (blue down triangle) and extensional part (green square) and sum (red circle) as a function of strain ($\boldsymbol{\gamma}$). Black solid line displays normal stress difference $\boldsymbol{\tau_{11} - \tau_{33}}$ ($\mathbf{N1 + N2}$).

As mentioned in the previous part, because of the bond length dependent inter-particle potential, the above equation is not applicable to our work. Therefore, we compared $2g_0^2 - g_1^2$ to $\tau_{11} - \tau_{33}$. To compare $2g_0^2 - g_1^2$ to $\tau_{11} - \tau_{33}$, $2g_0^2 - g_1^2$ was averaged in compressional part and extensional part, which are denoted by dotted lines in Figure. 4.2.7 (A). Because both of compressional part (negative $2g_0^2 - g_1^2$ and positive $\left(\frac{d\phi}{dr}\right)$ due to repulsive force by surface potential) and extensional part (positive $2g_0^2 - g_1^2$ and negative $\left(\frac{d\phi}{dr}\right)$ due to attractive force by bonding potential) contribute negatively to $\tau_{11} - \tau_{33}$, we compared the sum of $-\left|2g_0^2 - g_1^2\right|_{avg}$ in the compression part and extension part to $\tau_{11} - \tau_{33}$. Figure. 4.2.7 (B) shows the evolution of $-\left|2g_0^2 - g_1^2\right|_{avg}$ and $\tau_{11} - \tau_{33}$ as a function of strain (γ). $-\left|2g_0^2 - g_1^2\right|_{avg}$ in the compression part, where $2g_0^2 - g_1^2$ describes the structure along the velocity axis, shows undershoot behavior. The undershoot of $-\left|2g_0^2 - g_1^2\right|_{avg}$ in the compression part can be understood in connection with the structural rupture along the velocity axis. On the other hand, $-\left|2g_0^2 - g_1^2\right|_{avg}$ in the extension part does not exhibit clear undershoot behavior. Given that the $2g_0^2 - g_1^2$ in the extension part describes the structure along the vorticity direction, the unclear undershoot behavior can be understood as a result of relatively well maintained structure along the vorticity axis. The undershoot of the sum of $-\left|2g_0^2 - g_1^2\right|_{avg}$ in compression part and extension part qualitatively corresponds to the undershoot of the normal stress difference $\tau_{11} - \tau_{33}$, signifying close correlation between structural anisotropy and the rheological response.

4.2.3 Structural anisotropy in the gradient-vorticity plane

In Figure. 4.2.8, the pair distribution function difference Δg, structure factor difference ΔS, and particle configuration of the colloidal gel in the gradient $(\boldsymbol{\nabla v})$–vorticity $(\boldsymbol{\nabla \times v})$ plane are shown. The result in the gradient $(\boldsymbol{\nabla v})$–vorticity $(\boldsymbol{\nabla \times v})$ plane has much in common with the result in the velocity $(\boldsymbol{v})$-vorticity $(\boldsymbol{\nabla \times v})$ plane. As strain increases, innermost ring of the pair distribution function difference in the top row shows decrease along the gradient direction. Whereas, in the vorticity direction, the innermost ring exhibits comparatively slight decrease in the pair distribution function. The partial structural change, which results in structural anisotropy along the vorticity axis, is demonstrated in the structure factor difference as well. In the middle row of Figure. 4.2.8, as strain increases, the structure factor difference displays increase in intensity along the gradient axis, which is described by butterfly pattern. The butterfly pattern is similar to that in the velocity $(\boldsymbol{v})$-vorticity $(\boldsymbol{\nabla \times v})$ plane and can be interpreted as the structural anisotropy along the vorticity axis.

Figure. 4.2.9 shows the angular variation of the pair distribution function $g(2, \theta_{23})$ and the structure factor $S(q^*, \varphi_{23} + 90°)$. At equilibrium state of strain 0, the pair distribution function and the structure factor show flat curves, which indicate isotropic structure of the colloidal gel. At strain 0.2, the pair distribution function and the structure factor do not show any remarkable change. As strain increases further, near the gradient axis ($\theta_{23} = \varphi_{23} + 90° = 0°$ or $180°$), decrease in the pair distribution function is observed. On the other hand, near the vorticity axis ($\theta_{23} = \varphi_{23} + 90° = 90°$), the pair distribution function undergoes comparatively small decrease and shows maximum value, which indicates the structural anisotropy along the vorticity axis. In addition, the structure factor shows similar change, which shows the maximum value near the vorticity axis. This evolution of the structural anisotropy along the vorticity axis in the gradient $(\boldsymbol{\nabla v})$–

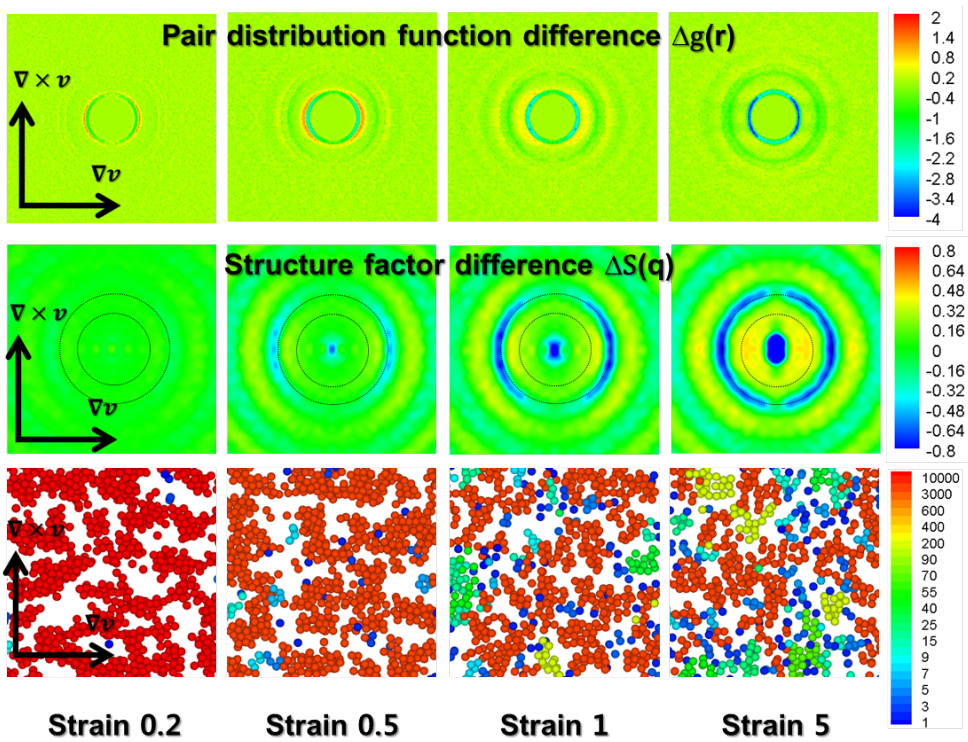

Figure. 4.2.8. Pair distribution function difference $\left(\Delta g(\vec{\mathbf{r}},\gamma) = g(\vec{\mathbf{r}},\gamma) - g(\vec{\mathbf{r}},\gamma = 0)\right)$ (top row) and Structure factor difference $\left(\Delta S(\vec{\mathbf{q}},\gamma) = S(\vec{\mathbf{q}},\gamma) - S(\vec{\mathbf{q}},\gamma = 0)\right)$ (middle row) in gradient($\boldsymbol{\nabla v}$)–vorticity($\boldsymbol{\nabla \times v}$) plane. Snapshots of the particle configuration. (bottom row) The images show the particles in the velocity-gradient plane sliced with a thickness of 4a. The color indicates the size of the cluster to which the particles belong. The black circles in the structure factor difference indicate the regime corresponding to the nearest neighbor structure.

vorticity $(\boldsymbol{\nabla} \times \boldsymbol{v})$ plane looks like that in the velocity $(\boldsymbol{v})$-vorticity $(\boldsymbol{\nabla} \times \boldsymbol{v})$ plane. In the velocity $(\boldsymbol{v})$-vorticity $(\boldsymbol{\nabla} \times \boldsymbol{v})$ plane, the evolution of the structural anisotropy along the vorticity axis is understood as a result of the shear-induced structural rupture, which causes the structural change near the velocity axis. Likewise, in the gradient $(\boldsymbol{\nabla v})$–vorticity $(\boldsymbol{\nabla} \times \boldsymbol{v})$ plane, the evolution of the structural anisotropy along the vorticity axis can be explained in the same way. The shear-induced structural rupture, which is preferred in the extensional direction, gives rise to structural change not only in the velocity direction but also in the gradient direction. However, due to the absence of vorticity direction component in shear flow, the shear flow does not have much effect on the structure in the vorticity direction. This makes the attractive particle interaction dominant in the vorticity direction and colloidal gel undergoes less microstructural change, which results in the structural anisotropy along the vorticity direction.

The anisotropic structure in the gradient$(\boldsymbol{\nabla v})$–vorticity$(\boldsymbol{\nabla} \times \boldsymbol{v})$ plane can be described by the linear combination of spherical harmonic terms, $\boldsymbol{2X_0^2 + X_1^2}$, which is shown in the inset of Figure. 4.2.10 (A). In Figure. 4.2.10 (A), $\boldsymbol{2g_0^2 + g_1^2}$, which denotes the intensity of $\boldsymbol{2X_0^2 + X_1^2}$, is shown as a function of distance, *r*. At strain 0, $\boldsymbol{2g_0^2 + g_1^2}$ exhibits flat curve, due to the isotropic structure at equilibrium state. As strain increases, at $\boldsymbol{r \cong 2}$ and in between 2 and 2.15, two peaks are observed. At $\boldsymbol{r \cong 2}$, the peak shows negative minima, which describes the structure along the gradient axis. As strain increased, the peak around $\boldsymbol{r \cong 2}$ gradually disappears. This disappearance indicates that the structure along the gradient direction is ruptured. In between 2 and 2.15, the peak shows positive maxima, which demonstrates the structure along the vorticity direction. In contrast to the peak at $\boldsymbol{r \cong 2}$, which exhibits gradual decrease due to the structure rupture along the gradient axis, the peak in between 2 and 2.15 maintains its value except for initial decrease. This signifies that the structure along the vorticity direction experiences less microstructural change.

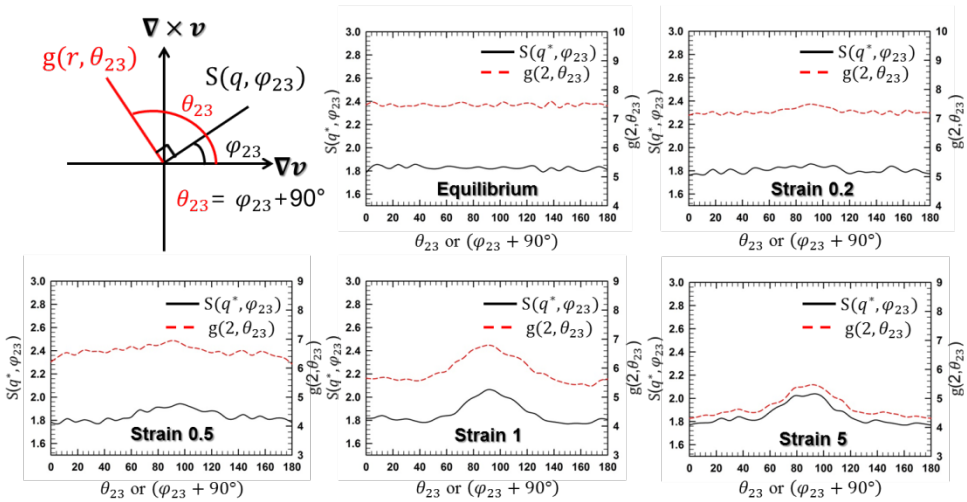

Figure. 4.2.9. Angular variation of pair distribution function ($\mathbf{g(2, \theta_{13})}$) and structure factor $\mathbf{S(q^*, \varphi_{13} + 90°)}$ in the gradient($\boldsymbol{\nabla v}$)–vorticity($\boldsymbol{\nabla \times v}$) plane

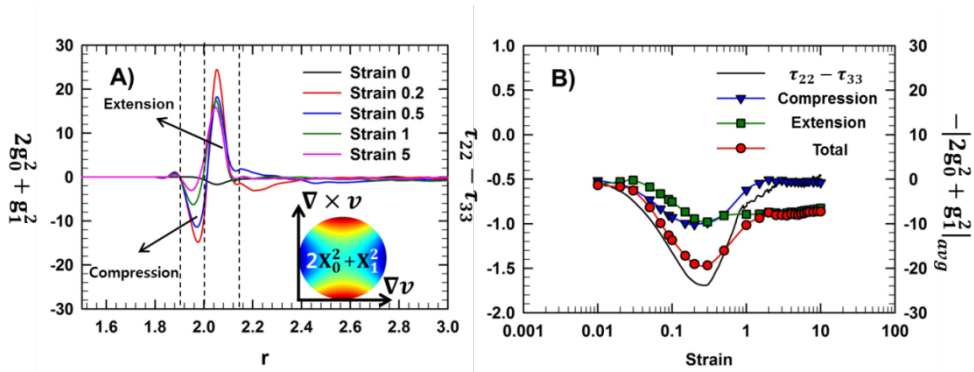

Figure. 4.2.10. A) A combination of spherical harmonic functions $\mathbf{2X_0^2 + X_1^2}$ (Inset) and coefficients $\mathbf{2g_0^2 + g_1^2}$, which correspond to the structural anisotropy along vorticity direction in gradient ($\boldsymbol{\nabla v}$)–vorticity ($\boldsymbol{\nabla \times v}$) plane. Dotted lines denote the compression part and the extension part. **B)** Absolute value of $\mathbf{2g_0^2 + g_1^2}$ averaged over compressional part (blue down triangle) and extensional part (green square) and sum (red circle) as a function of strain ($\boldsymbol{\gamma}$). Black solid line displays normal stress difference $\boldsymbol{\tau_{22} - \tau_{33}}$ (**N2**).

The analysis through the spherical harmonic expansion of the pair distribution function signifies that the structural anisotropy in the gradient ($\mathbf{\nabla v}$)-vorticity ($\mathbf{\nabla \times v}$) plane is closely linked to the second normal stress difference $\tau_{22} - \tau_{33}$. Theoretically, the relationship between $2g_0^2 + g_1^2$ and $\tau_{22} - \tau_{33}$ is given as follows [67]

$$\tau_{22} - \tau_{33} = \frac{2}{15}\pi\rho^2 \int_0^\infty r^3 (2g_0^2 + g_1^2)\left(\frac{d\phi}{dr}\right) dr. \quad (4.3)$$

As the above equation is not directly applicable to our work, we analyzed the correlation between the anisotropic structure and the second normal stress difference by comparing $2g_0^2 + g_1^2$ to $\tau_{22} - \tau_{33}$. To compare $2g_0^2 + g_1^2$ to $\tau_{22} - \tau_{33}$, $2g_0^2 + g_1^2$ was averaged in compressional part and extensional part, respectively. Because both of the compression part (negative $2g_0^2 + g_1^2$ and positive $\left(\frac{d\phi}{dr}\right)$ due to repulsive force by surface potential) and the extension part (positive $2g_0^2 + g_1^2$ and negative $\left(\frac{d\phi}{dr}\right)$ due to attractive force by bonding potential) contribute negatively to $\tau_{22} - \tau_{33}$, we compared the sum of $-\left|2g_0^2 + g_1^2\right|_{avg}$ in the compression part and the extension part to $\tau_{22} - \tau_{33}$. Figure. 4.2.10 (B) shows the evolution of $-\left|2g_0^2 + g_1^2\right|_{avg}$ and $\tau_{22} - \tau_{33}$ as a function of strain. In the case of compression part, where negative $2g_0^2 + g_1^2$ describes the anisotropic structure along the gradient axis, $-\left|2g_0^2 + g_1^2\right|_{avg}$ shows undershoot, which can be ascribed to the structural rupture along the gradient axis. On the other hand, in the extension part, where positive $2g_0^2 + g_1^2$ is related to the anisotropic structure along the vorticity axis, $-\left|2g_0^2 + g_1^2\right|_{avg}$ rarely shows undershoot. As in the velocity ($\boldsymbol{v}$)-vorticity ($\mathbf{\nabla \times v}$) plane, the absence of undershoot can be correlated to the maintenance of the structure in the vorticity axis. The sum of $-\left|2g_0^2 + g_1^2\right|_{avg}$ in the compression part and the extension part demonstrates undershoot behavior, which corresponds to the undershoot of $\tau_{22} - \tau_{33}$.

4.3. Modified stress-SANS rule

So far, the shear-induced anisotropic structure of the colloidal gel has been quantitatively analyzed through the pair distribution function and the structure factor. The analysis through the pair distribution function is intuitive and easily understandable. Especially, the spherical harmonic expansion of the pair distribution function shows close connection between the structural anisotropy and rheological behavior. However, the analysis through the pair distribution function is possible only in case that the information on position of the all the particles is available. Even though late improvement of the experimental techniques, for example confocal microscopy, has made it possible to measure the particle position, it is still hard to get the information on the particle position. Therefore, in experimental studies, the structural anisotropy is usually studied through analysis of scattering pattern, which corresponds to the structure factor in this study. In this part, the structure factor will be further analyzed and correlated to the stress response, which is expected to provide useful information for experimental approach.

In the analysis of structure factor, the structural anisotropy can be quantified using the alignment factor (A_f) given as the Eq. (2.29). Figure. 4.3.1 (A) shows normalized shear stress ($\tau_{12}/\tau_{12,max}$), alignment factor ($A_f/A_{f,max}$), and average bond number (z/z_{max}) change under start-up shear of Pe 200. The alignment factors in all three planes show overshoot behavior as the shear stress. In the velocity ($\boldsymbol{v}$)-gradient ($\boldsymbol{\nabla v}$) plane, where the structural anisotropy in the compressional axis direction is observed, the alignment factor A_{f12} increases as soon as the shear flow is applied. However, in the velocity ($\boldsymbol{v}$)-vorticity ($\boldsymbol{\nabla \times v}$) plane and the gradient ($\boldsymbol{\nabla v}$)-vorticity ($\boldsymbol{\nabla \times v}$) plane where the colloidal gel shows the structural anisotropy along the vorticity direction, the alignment factor does not increase instantly and displays delayed increase. This can be attributed to the difference in structural anisotropy-inducing mechanism.

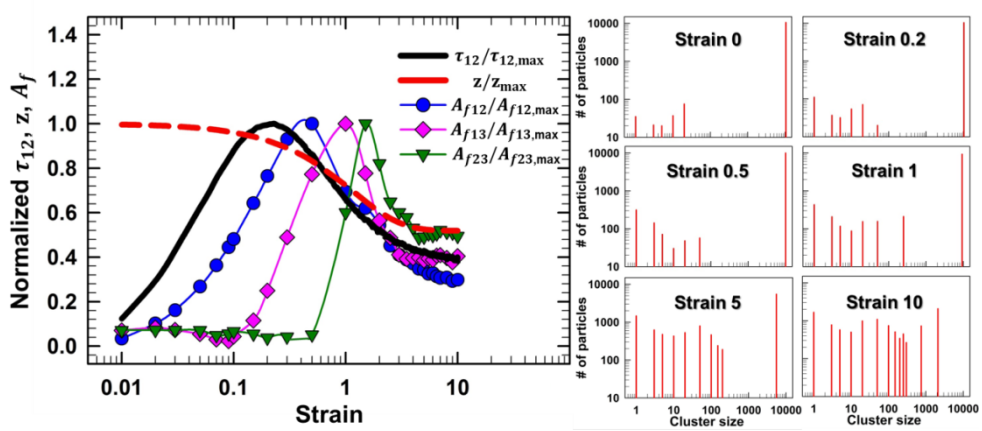

Figure. 4.3.1. A) Normalized shear stress ($\tau_{12}/\tau_{12,max}$ (black solid line)), average bond number (z/z_{max} (red dashed line), and alignment factors ($A_{f12}/A_{f12,max}$ (blue circle), $A_{f13}/A_{f13,max}$ (pink diamond), $A_{f23}/A_{f23,max}$ (green triangle)) at Pe 200. **B)** Particle number distribution according to the cluster size at each strain at Pe 200.

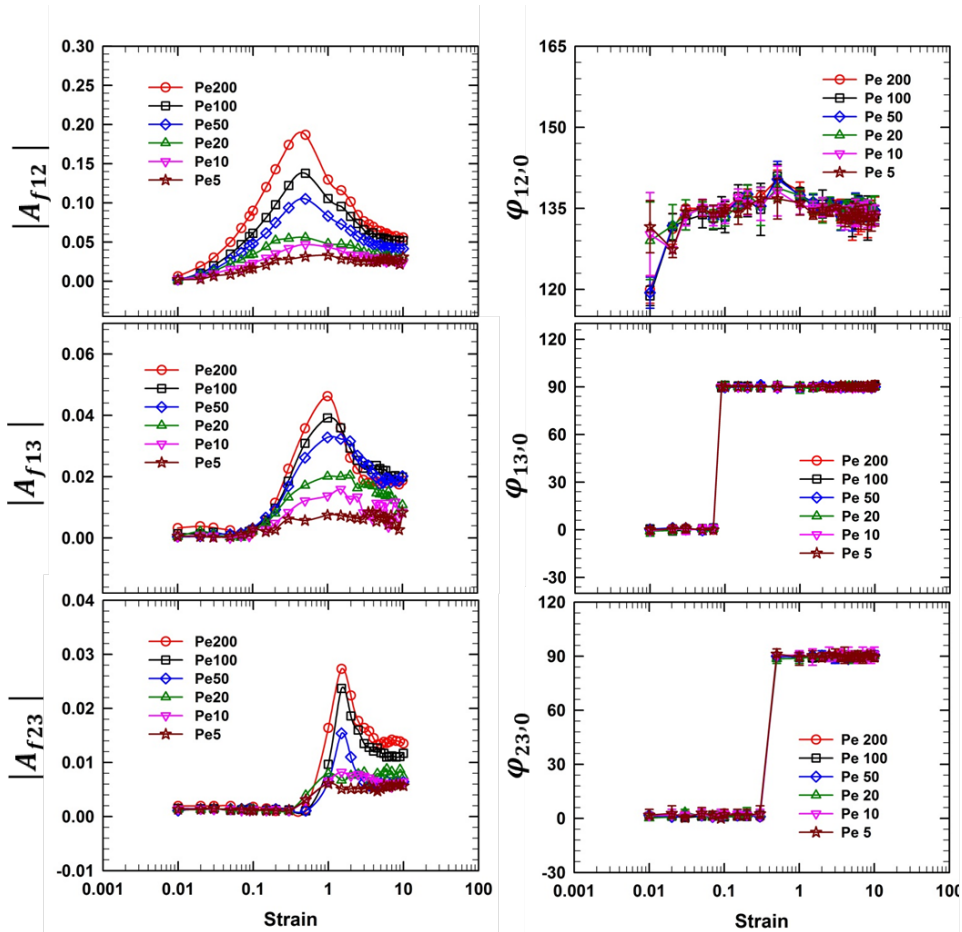

Figure. 4.3.2. Alignment factor $(A_{f12}, A_{f13}, A_{f23})$ change and principal axis angle $(\varphi_{12,0},\ \varphi_{13,0}, \varphi_{23,0})$ change in velocity (v)-gradient (∇v) plane, velocity (v)-vorticity$(\nabla \times v)$ plane, and gradient(∇v)- vorticity$(\nabla \times v)$ plane.

In the velocity $(\boldsymbol{v})$-gradient $(\boldsymbol{\nabla v})$ plane, the structural anisotropy can be caused not only by the structural breakup which depletes the particles along the extensional axis but also by the structural deformation which condenses the particles along the compressional axis. Therefore, the initial strain increase without remarkable bond breaking can cause the increase in A_{f12}. Indeed, in Figure. 4.3.1 (A), while the average bond number does not show remarkable change in the beginning of start-up shear, the alignment factor in the velocity-gradient plane A_{f12} demonstrates clear increase. In contrast, according to the angular variation of the pair distribution function and the structure factor, it has been shown that the structural anisotropy along the vorticity axis is induced by structural rupture, which prefers the velocity and gradient direction. This being so, the initial structural deformation without bond breaking does not increase the alignment factor in the velocity-vorticity plane and the gradient-vorticity plane. As shown in the Figure. 4.3.1 (A), the delayed increase in alignment factors A_{f13} and A_{f23} accompanies rupture of colloidal gel structure, which is represented by the decrease in the average bond number.

As strain increases further, the colloidal gel shows decrease in the alignment factors in all three planes. The decrease in the alignment factor is linked to the structural change from the percolated network to small fragments. Figure. 4.3.1 (B) shows the particle number distributions according to the cluster size. Here, abscissa represents the size of the cluster to which the particles belong and ordinate indicates the number of the particles belonging to each cluster size, which is the product of cluster size and the number of clusters. At strain 0, the particle number distribution shows a big peak around 10,000, which describes the percolated network chain. Under the start-up shear flow, the peak is maintained until strain 1 and this indicates that the colloidal gel maintains the network structure. However, at higher strain, this big peak shrinks and moves to left. In addition, there appears several peaks in the cluster size of dozens to hundreds. This delineates the structural change from percolated network to several clusters and flocs. As the anisotropic gel structure turns into isotropic fragments, the alignment factors in the

velocity ($\boldsymbol{v}$)-vorticity ($\boldsymbol{\nabla} \times \boldsymbol{v}$) plane and the gradient ($\boldsymbol{\nabla v}$)-vorticity ($\boldsymbol{\nabla} \times \boldsymbol{v}$) plane decrease. This result corresponds with the change of the angular variation of the pair distribution function and the structure factor, which shows the decrease in the structural anisotropy with the overall decrease of the pair distribution function and the structure factor. The colloidal gel shows similar alignment overshoot behaviors at various Pe as shown in Figure. 4.3.2 .

The overshoot of the alignment factor can be linked to the stress response by the stress-SANS rule [68]

$$\sigma = G_0\left[C(\dot{\gamma})A_{f12}\right]^{1/2}\sin\left(2\varphi_{12,0}\right). \tag{4.4}$$

Here, G_0 and $C(\dot{\gamma})$ are shear modulus and the stress-SANS coefficient which is defined from steady shear measurement. Usually, the stress-SANS rule has been applied to systems such as micellar solution [69,70], which is assumed to have the polymeric contribution to rheological behavior. In this work, assuming that the network structure of the colloidal gel also has similar polymeric contribution to rheological property, we applied the stress-SANS rule to quantitatively associate the structural anisotropy to rheological behavior. In Figure. 4.3.3, comparison between the measured shear stress and the shear stress prediction by stress-SANS rule at various Pe is shown. The red solid line denotes the measured stress and pink triangle indicates the stress-SANS calculation with $C(\dot{\gamma})$ defined from the steady shear measurement. The stress-SANS rule seems to predict the stress response of the colloidal gel to some extent. The stress-SANS rule with $C(\dot{\gamma})$ from the steady shear measurement correctly describes the stress response at large strain near the steady state. However, the stress-SANS calculation does not correctly predict the linear stress responses at small strain, showing smaller stress prediction. In addition, the linear to non-linear rheological transition which is manifested as the stress overshoot, is not properly described. The stress-SANS results shows smaller maximum stress and the mismatch of the strains, where the maximum stress is observed. The poor performance in the linear regime seems to be a result of using

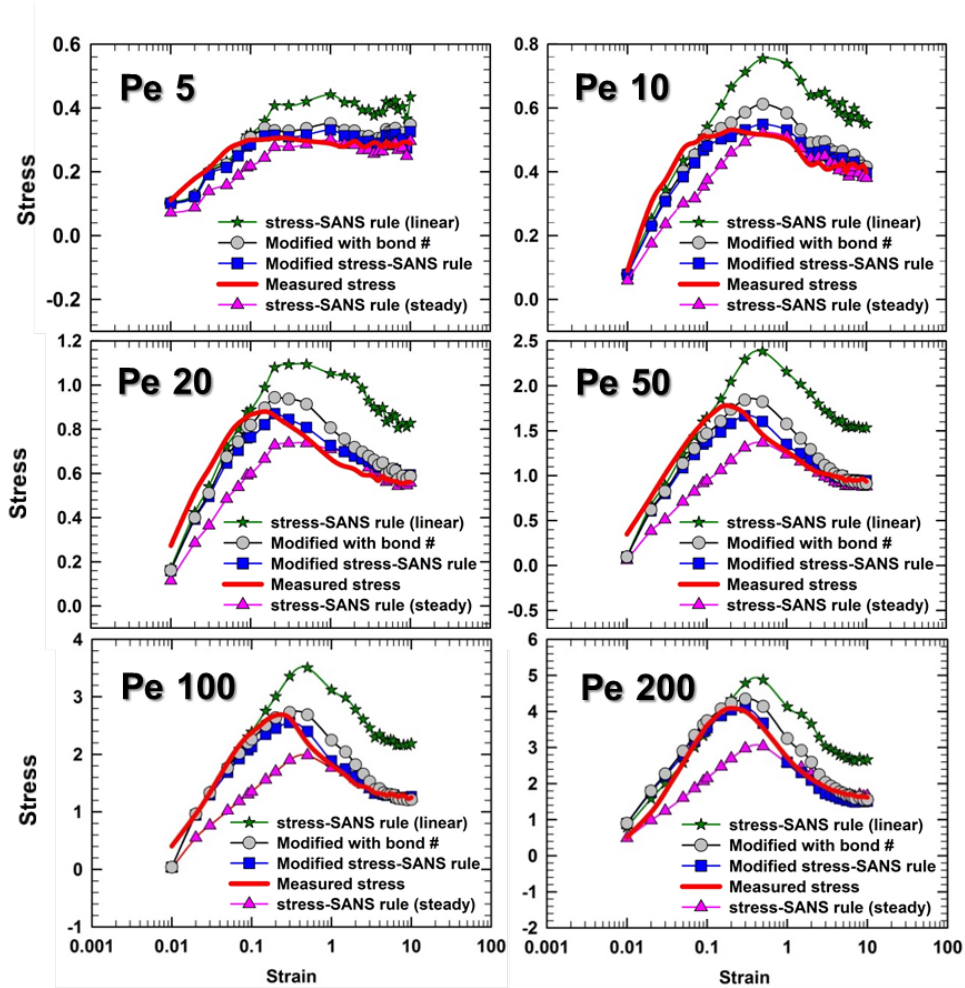

Figure. 4.3.3. Measured and predicted stress responses of the colloidal gel at various Pe. Stress responses are predicted using Stress SANS rule and modified Stress SANS rule. Stress-SANS (Linear) indicates the use of the stress SANS coefficients defined on the basis of linear rheological behaviors. In the case of stress-SANS (steady), steady shear measurements are used to define the stress SANS coefficients. Modification (bond number) signifies the modified stress-SANS rule in which structure parameter(λ) is replaced with normalized average bond number $\left(\frac{z(\gamma)}{z_{init}}\right)$.

$C(\dot{\gamma})$ from the steady shear measurement, which is set on the basis of steady shear measurements. Therefore, instead of defining $C(\dot{\gamma})$ from the steady shear measurement, we introduced a new stress-SANS coefficient based on the linear rheological behavior. We newly defined $C(\dot{\gamma})$ to minimize the deviations from the linear rheological behavior at small strain, before the stress maximum. The green stars denote the stress-SANS calculation with $C(\dot{\gamma})$ defined on the basis of the linear rheological behavior. With the newly defined coefficient $C(\dot{\gamma})$, the stress-SANS rule correctly predicts the linear stress response at small strain. However, compared with the measured stress response, the stress-SANS calculation still shows stress maximum at larger strain and the stress responses after the stress maximum are not described correctly.

The failure of the stress-SANS rule can be discussed in terms of the structural rupture during the startup shear flow. As opposed to the stress-SANS rule, in the analysis with the pair distribution function, theoretical prediction through the spherical harmonic expansion shows close connection between the structural anisotropy and rheological behavior. This difference comes from the definition of the alignment factor. The pair distribution function and its spherical harmonic expansion involve the information on the size-related structural change, such as breakup of the bonding, as well as structural anisotropy. On the other hand, as it is divided by angular averaged intensity as given in Eq. (2.29), the alignment factor does not include the information on the size-related structural change. In respect that the size-related structural changes play an important role in determining the strength of the material, the stress-SANS rule cannot depict the nonlinear rheological behaviors such as stress overshoot, which accompanies rupture of the colloidal gel structure [19, 20]. As an alternative, we introduce the structure kinetics model to stress-SANS rule and suggest a modified stress-SANS rule. The structure kinetics model is commonly used in theoretical studies to describe the thixotropic materials [56]. Constitutive equations, which link a stress response to a microstructure, employ structure kinetics model to include the influence of the microstructural change. In the structure kinetics model, the instantaneous structure

is represented by a dimensionless scalar parameter λ, which is called structure parameter. The time dependence of λ is described by a differential equation, evolution equation. The evolution equation links the time rate of change of the structure (λ) to the instantaneous flow conditions and microstructure.

Adopting the structure parameter, the modified stress-SANS rule can be proposed in the form of

$$\sigma = S\lambda \times \left(\dot{\gamma}^{1/2}\right) \times \left[{A_{f12}}^{1/2} \sin\left(2\varphi_{12,0}\right)\right]. \tag{4.5}$$

Here, the first term on the right-hand side $S\lambda$ corresponds to G_0 in original stress-SANS rule. In the original stress-SANS rule, G_0, which represents the structural strength, is given as a constant and independent of strain and shear rate. Therefore, the structural change of colloidal gel, which has a profound effect on the stress response, cannot be considered in the original stress-SANS rule. However, in the modified stress-SANS rule, the structural strength is described by product of a material constant S and the structure parameter λ. In the Eq. (4.5), the material constant S represents the strength of the colloidal gel network structure at equilibrium state. By multiplying S by the structure parameter λ, which describes the structural change of colloidal gel, the influence of the structural change on the stress response can be considered. The structure parameter is given as the solution of the following evolution equation,

$$\frac{d\lambda}{dt} = -k_1|\dot{\gamma}|\lambda + k_2|\dot{\gamma}|^{0.5}(1-\lambda). \tag{4.6}$$

Here, the first term on the right-hand side describes the shear-induced breakup and the second term on the right-hand side expresses shear-induced structure buildup. The analytic solution of the Eq. (4.6) is given by

$$\lambda = \left(\frac{k_2|\dot{\gamma}|^{0.5}}{k_1|\dot{\gamma}|+k_2|\dot{\gamma}|^{0.5}}\right) + \left(\frac{k_1|\dot{\gamma}|}{k_1|\dot{\gamma}|+k_2|\dot{\gamma}|^{0.5}}\right) \times \exp\{-(k_1|\dot{\gamma}| + k_2|\dot{\gamma}|^{0.5}) \times t\}. \tag{4.7}$$

To use the modified stress-SANS rule, three material constants of S, k_1, k_2 should be determined. In this work, the three constants were determined through the curve

fitting with the result in Figure. 4.3.2. The first row in the Figure. 4.3.2 shows the evolutions of the alignment factor A_{f12} and the principal axis angle $\varphi_{12,0}$ in the velocity($\boldsymbol{v}$)-gradient($\boldsymbol{\nabla v}$) plane at various Pe (5, 10,20, 50, 100, 200). With the evolution results, the best fitting parameters ($S = 0.025, k_1 = 1.14, k_2 = 15.89$), which fits the measured stress best for all Pe, were chosen using the polynomial curve fitting technique and the least square approach. In the middle of the right hand side, the influence of the shear rate, which is described by stress-SANS coefficient $C(\dot{\gamma})$ in the original stress-SANS rule, is represented by $\dot{\gamma}^{1/2}$. Because the shear rate is closely related with relaxation of the structure, the stress response of the colloidal gel depends on the applied shear rate. In Figure.4.1.1 (D), it has been shown that the flow curve of the colloidal gel conforms to the SGR model, which predicts the power law relationship between shear rate and steady shear stress with an exponent of 0.5. In addition, the stress overshoot in Figure.4.1.1 (C) agrees with the SGR model, which demonstrates the stress maximum at a constant strain. Therefore, according to these similarities, the influence of the shear rate on the stress response is represented based on the SGR model, which expects the power law increase of the shear stress with an exponent of 0.5 under start up shear [61]. The last term ${A_{f12}}^{1/2} \sin(2\varphi_{12,0})$, which describes the influence of the structural anisotropy, is unchanged.

In Figure. 4.3.3, blue squares show the stress response calculated by the modified stress-SANS rule. Interestingly, the modified stress-SANS rule demonstrates better performance in all strain. The modified stress-SANS rule correctly predicts the stress responses both at small strain and large strain. Moreover, the strain, where the stress reaches maximum, is correctly predicted, compared with the original stress-SANS rule. To verify the correlation between the structure parameter calculated from structure kinetics model and the colloidal gel structure, we introduced another structure index to stress-SANS rule. Theoretically, the structure parameter has been associated with the number of links between structure elements, for example bonds between the particles. According to this, the

structure parameter was replaced with a normalized average bond number $\frac{z(\gamma)}{z_{init}}$. Here, z_{init} and $z(\gamma)$ note the average bond number at initial equilibrium state and at strain γ, respectively. The gray circles in Figure. 4.3.3 shows the stress responses calculated from the stress-SANS rule, which was modified with the average bond number. The stress-SANS rule modified with the average bond number shows the stress response, which is very similar to the stress-SANS rule with the structure kinetics model. This result verifies the correlation between the structure parameter and colloidal gel structure. The modified stress-SANS rule can be usefully employed in the studies through scattering analysis, especially, where the material undergoes structural changes such as structural rupture under the flow condition.

Chapter 5. Structural change and dynamics of colloidal gel under oscillatory shear flow

5.1. Structural change under oscillatory shear flow

Figure. 5.1.1 shows the microstructures of the colloidal gels at maximum strain. The abscissa and the ordinate indicate the strain amplitude and frequency, respectively. In this work, the frequency is presented as a non-dimensionalized Peclet number ($\mathrm{Pe}_\omega = \omega\tau_r$), which is the product of the angular frequency (ω) and the characteristic time (τ_r) defined in the previous section. Depending on the flow condition, the colloidal gel shows different structural changes. Regardless of the frequency, at small strain amplitudes, most particles are red, which implies that the colloidal gel maintains its network structure without remarkable structural change. However, at large strain amplitude, 50% and 100%, depending on the frequency, different structural change is observed. At low frequency $\mathrm{Pe}_\omega = 100$, even when the strain amplitude is increased to 100%, the overall network structure is maintained. Nevertheless, the network strands become thinner, which is represented quantitatively by the average bond number decrease in Figure. 5.1.1. At frequency of $\mathrm{Pe}_\omega = 500$, as the strain amplitude increases beyond 50%, the colloidal gel starts to break-up into several clusters. Similarly, at high frequency of $\mathrm{Pe}_\omega = 2000$, the increase in strain amplitude results in the rupture of the network structure into small clusters. However, at this high frequency regime, the clusters further breakup into smaller flocs which are colored green and blue in Figure. 5.1.1. These structural changes can be attributed to different flow conditions which are closely related to the relaxation of flow-induced structural deformation and bond reformation [20, 25, 45]. At low frequency, although the imposed large strain deforms the colloidal gel leading to thinner chains, the bond reformation makes it possible to maintain the network structure. However, at high frequency, the colloidal gel is not given enough time for bond reformation. To understand the structural change in local length scale, we calculated the average bond number (z_{avg}) and the bond number distribution change relative to the initial bond number distribution ($\mathrm{P}(z)_{avg} - \mathrm{P}(z)_{init}$). The average bond number was

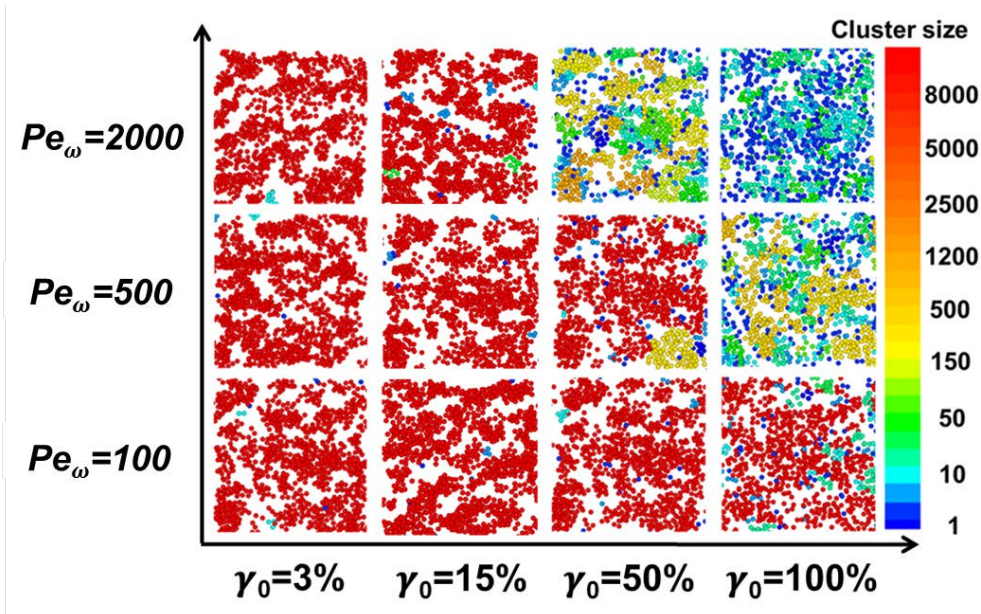

Figure. 5.1.1. Structure of a deformed colloidal gel under oscillatory shear flow at maximum strain. The images show the particles at the center of the simulation box (sliced with a thickness of 6a in the flow-shear gradient (x-y) plane). The color indicates the size of the cluster to which the particles belong.

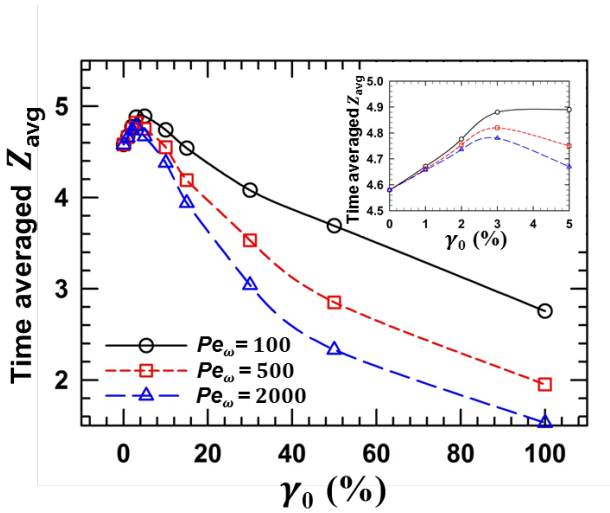

Figure. 5.1.2. Time-averaged (during one oscillating cycle) bond number (z_{avg}) as a function of strain amplitude (γ_0). Inset shows the time-averaged bond number change at small strain amplitude regime.

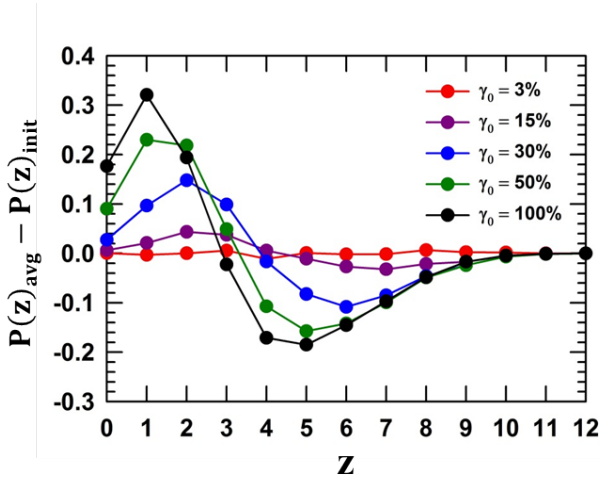

Figure. 5.1.3. Time-averaged (during one oscillating cycle) bond number distribution ($\mathbf{P}(z)_{avg}$) change relative to the initial bond number distribution ($\mathbf{P}(z)_{init}$) at frequency $\mathbf{Pe}_{\omega} = \mathbf{2000}$.

calculated by dividing the sum of the bond number of the particles by the number of particles. Figure. 5.1.2 shows z_{avg}, averaged over one oscillating cycle, as a function of strain amplitude. At small strain amplitude around 3~5%, a slight increase of z_{avg} is observed. It can be considered as a result of shear induced restructuring of the colloidal gel which promotes the aggregation of the particles at low shear rate.As the strain amplitude increases further, the z_{avg} starts to decrease, which indicates that the yielding can be regarded as a transition from multiply-connected rigid chains to singly-connected soft chains [20]. In Figure. 5.1.3, the change in bond number distribution ($\mathrm{P}(z)_{avg} - \mathrm{P}(z)_{init}$) relative to the initial bond number distribution is shown. As the strain amplitude increases, the fraction of the particles with bond number larger than or equal to 4 decreases, while that of the particles with bond number lower than 4 increases. This structural change corresponds well with that of the previous studies on the start-up of shear flow in which the yielding behavior of the colloidal gel was regarded as a topological change from rigid to soft chains [19, 20]. In these studies, the yielding behavior of the colloidal gel was analyzed in terms of the characteristics of the rigid and soft chains. In previous studies [17, 18, 53], the origin of the elasticity has been attributed to the rigid chain structure. Here, the rigid chain indicates the network structure with high bond number. The particles with high bond number experience a slow relaxation. Therefore, the particles with high bond number resists against the external deformation supporting the stress. On the other hand, the particles with low bond number experiences fast relaxation and cannot support the stress. Theoretically and experimentally, it has been shown that the criterion for rigidity is the bond number 4, when there is non-central force between the particles as in this work [15, 19]. The structural change in this work, the decrease in the particles with bond number larger than or equal to 4 and the increase in the particles with bond number lower than 4, can be understood in the same vein with the previous work. In addition, the observed structural change can be associated with other modeling work. Sticky particle model [58] was employed to study the structural change of attractive particle suspension under the steady shear flow. Under the shear flow, the

clusters were disaggregated forming string-like soft chains. The structural changes with sticky particle model can be understood in the context of a transition from rigid chain to soft chain as in this work.

The structural change from rigid to soft chains is directly manifested in the rheological behavior. Figure. 5.1.4 shows the storage modulus (G′) and loss modulus (G″) as a function of strain amplitude. They were calculated in the strain amplitude range in which the colloidal gel shows a clear and reasonable stress response. (for example, at $Pe_{\omega} = 100$, it is hard to get a clear stress curve at strain amplitude lower than 3%) In the small amplitude oscillatory shear (SAOS) (strain amplitude from 0 to 10%), where the rigid chain network is maintained, both G' and G" are almost constant. However, at the medium amplitude oscillatory shear (MAOS) (strain amplitude ~15%), where the structural change from rigid chain structure (with bond number larger or equal to 4) to soft chain structure (with bond number lower than 4) begins to occur, both G′ and G″ start to decrease. In the large amplitude oscillatory shear (LAOS), G′ and G″ decrease as the fraction of the rigid chains decreases.

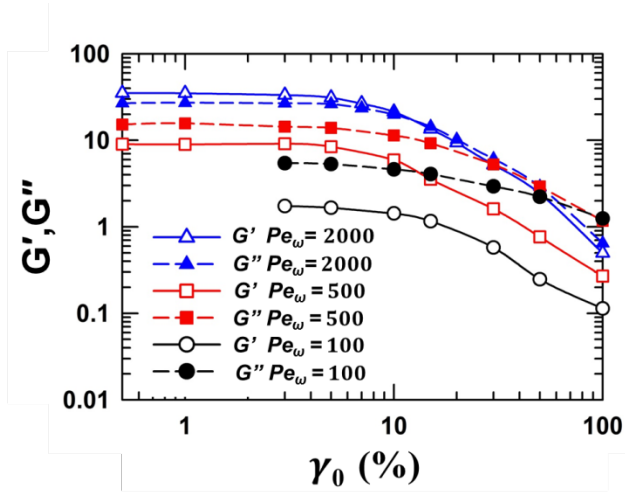

Figure. 5.1.4. G′ and G″ as a function of strain amplitude (γ_0).

5.2. Dynamics of colloidal gel under oscillatory shear flow

5.2.1. SAOS (Small amplitude oscillatory shear) regime

First, we focus on the dynamics of the colloidal gel in the SAOS regime. Figure. 5.2.1 shows the stress, strain and average bond number in the SAOS regime at a strain amplitude of 3%. The red short-dashed line, black solid line, and blue long-dashed line represent the normalized stress, strain, and average bond number, respectively, in one cycle. At a strain amplitude of 3%, the colloidal gel and displays linear behavior with a sinusoidal stress curve. During the oscillation, the average bond number shows a slight fluctuation and is negatively correlated with the absolute value of strain. As the strain deviates from strain 0 (from point 1 to 3 and from point 5 to 7), the average bond number decreases, while the average bond number increases as the absolute value of strain decreases (from point 3 to 5 and from point 7 to 1). On the right side of Figure. 5.2.1, the pair distribution functions projected onto the flow-gradient plane at every 1/8 oscillation cycle are given. The pair distribution projection was calculated for a slice of thickness *a* (particle radius) with the bin size of $\delta r = 0.01a$. In this regime, the colloidal gel shows no anisotropy during the oscillation. In the SAOS regime, it has been shown that the colloidal gel maintains the structure without remarkable structural change. The observed linear behavior with sinusoidal curve can be regarded as a consequence of the maintained rigid network structure.

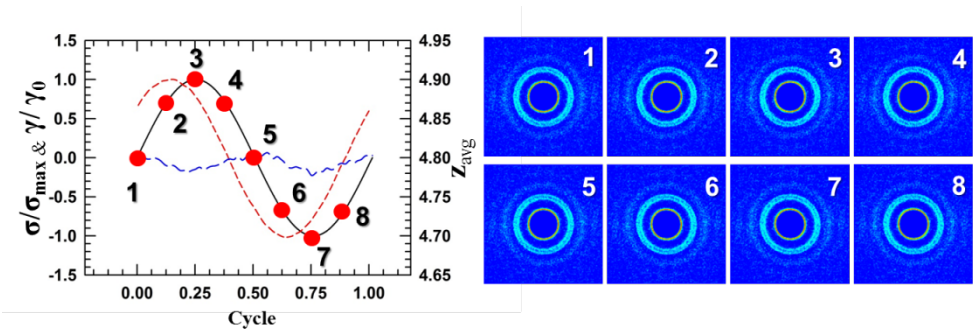

Figure. 5.2.1. Normalized stress (σ/σ_{max}, short dashed red line), strain ($\boldsymbol{\gamma}/\boldsymbol{\gamma}_0$, black solid line), and average bond number ($\boldsymbol{z_{avg}}$, long dashed blue line) during one oscillation in SAOS regime ($\boldsymbol{\gamma_0 = 3\%}$). Pair distribution functions at every 1/8 cycles (projected onto the flow-shear gradient (x-y) plane) are displayed at the position numbered on the strain curve.

5.2.2. MAOS (Medium amplitude oscillatory shear) regime

Secondly, the dynamics in the MAOS regime at strain amplitude of 15% will be discussed. In Figure. 5.2.2, the stress, strain, and average bond number change under oscillatory shear at a strain amplitude of 15% are shown. Different from the SAOS regime, the colloidal gel shows a clear structural oscillation of the average bond number. As the strain deviates from strain 0 (from point 1 to 3 and from point 5 to 7), the average bond number decreases, while the average bond number increases as the absolute value of strain decreases with the reverse flow (from point 3 to 5 and from point 7 to 1). The dynamics with the negative correlation between the absolute value of strain and the average bond number can be associated with the gel structure as described below. According to the structural change in previous section, a small number of rigid chain starts to break-up into singly-connected soft chains. Both rigid and soft chains coexist in this regime. However, the overall gel structure is still dominated by rigid chains. As the rigid chains resist deformation, the increase in strain will break them into a soft chain structure with less resistance. Therefore, as the absolute value of strain increases, the average bond number decreases. In the reverse flow, as the absolute value of strain decreases, the chain structure is recovered with the increase in the average bond number. This is well manifested in the rheological behavior. In Figure. 5.2.2, the colloidal gel shows nonlinear behavior with non-sinusoidal stress curve. The stress curve has a shoulder at the point where the average bond number reaches its maximum. The coincidence of these two points implies that the linear-to-nonlinear transition of the colloidal gel can be directly related to the rupture of the network structure. In this regime, as shown in Figure. 5.2.2, the colloidal gel shows an anisotropic structure. As the absolute value of strain increases, the anisotropy along the compressional axis is observed, which attributes to the structure break-up along the extensional direction. This result is quite similar with that in steady shear flow [20, 24, 36, 37].

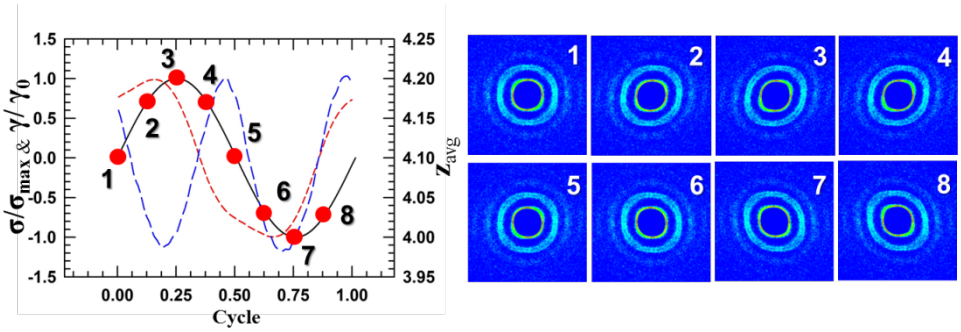

Figure. 5.2.2. Normalized stress (σ/σ_{max}, short dashed red line), strain ($\boldsymbol{\gamma}/\boldsymbol{\gamma}_0$, black solid line), and average bond number ($\boldsymbol{z_{avg}}$, long dashed blue line) during one oscillation in MAOS regime ($\boldsymbol{\gamma_0 = 15\%}$). Pair distribution functions at every 1/8 cycles (projected onto the flow-shear gradient (x-y) plane) are displayed at the position numbered on the strain curve.

As the absolute value of strain decreases by the reverse flow, the anisotropy decreases and the direction of anisotropy changes according to the strain change

5.2.3. LAOS (Large amplitude oscillatory shear) regime

Lastly, the dynamics in the LAOS regime at strain amplitude of 50% will be considered. In Figure. 5.2.3, the stress, strain, and average bond number of the colloidal gel under the oscillatory shear flow at strain amplitude 50% are presented. In this condition, the rigid network structure with high bond number is ruptured and the gel structure is dominated by the soft chains with low bond number. The structure shows different dynamics compared to the structure in the SAOS and MAOS regimes. In Figure. 5.2.3, as the strain deviates from strain 0 (from point 1 to 3 and from point 5 to 7), the average bond number increases, while the average bond number decreases as the absolute value of strain decreases with the reverse flow (from point 3 to 5 and from point 7 to 1). Compared to the MAOS where the average bond number is negatively correlated with the absolute value of strain, the positive correlation between the average bond number and the absolute value of strain is completely opposite to the previous case. In previous conditions where the gel structure is dominated by the rigid chains, the negative correlation between the absolute value of strain and the average bond number can be associated with the rupture of rigid chain structure which resists deformation. On the other hand, the positive correlation can be associated with the dynamics of soft chains which dominate the overall gel structure in the LAOS regime. Different from the rigid chain, the soft chain shows a floppy motion without resistance against deformation. In the previous study on the dilute colloidal gel with soft chain structure [29], the floppy motion of the soft chain led to the rotational motion and the bond formation between the soft chains. Therefore, the increase in the average bond number with the absolute value of strain can be ascribed to the shear induced cluster densification by the floppy motion of soft chains. In the reverse flow, the relatively rigid structure which is formed during the increase in the absolute value of strain becomes ruptured, leading to the decrease in the average bond number.

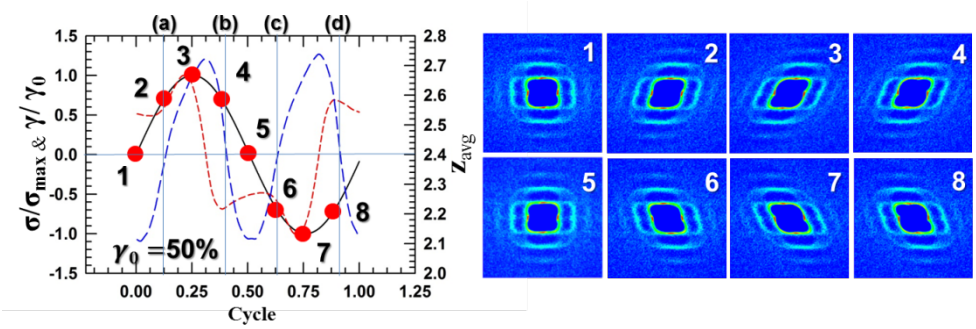

Figure. 5.2.3. Normalized stress (σ/σ_{max}, short dashed red line), strain ($\boldsymbol{\gamma}/\boldsymbol{\gamma}_0$, black solid line), and average bond number ($\boldsymbol{z_{avg}}$, long dashed blue line) during one oscillation in LAOS regime ($\boldsymbol{\gamma_0 = 50\%}$). Pair distribution functions at every 1/8 cycles (projected onto the flow-shear gradient (x-y) plane) are displayed at the position numbered on the strain curve.

In Figure. 5.2.3, the strain and the average bond number are not completely in phase. The average bond number shows a certain phase shift from the strain curve. This shift is observed in the MAOS regime as well. In Figure. 5.2.2, where the negative correlation is observed, they are not exactly in anti-phase. The phase shift can be attributed to the influence of some remaining rigid or soft chains. In the LAOS regime, the overall structure is dominated by the soft chains which are expected to lead in-phase of both the strain and the average bond number. However, there still exists some rigid chain structure, which is expected to show anti-phase behavior. Therefore, the influence of the remaining rigid structure can be manifested as a phase shift. In the same vein, the phase shift in the MAOS regime, in which the overall structure is dominated by the rigid chains, can be understood as an influence of the soft chains.

In Figure. 5.2.3, the colloidal gel shows a highly nonlinear stress response with several local maxima and minima. This stress curve is quite similar with that of the experiments where the microstructure and rheology of adhesive hard sphere colloidal gel under large amplitude oscillatory shear has been studied [36]. This highly nonlinear behavior can be related to the structural fluctuation under the oscillatory shear flow. In Figure. 5.2.3, the average bond number fluctuates between 2.1 and 2.7 with an average value of 2.4. In previous works [71, 72], an average bond number of 2.4 was suggested as a criterion for the rigidity percolation. Considering that this rigidity percolation is closely related to the elastic transition [72], the average bond number change around 2.4 is expected to have an effect on the rheological response of the colloidal gel. The stress curve in Figure. 5.2.3 confirms this expectation; at points (b) and (d), as the average bond number decreases below the rigidity percolation (~ 2.4), the colloidal gel loses the elasticity. This is represented by the local minimum (b) and the local maximum (d) of the stress, which shows a sudden decrease of the stress. On the other hand, at points (a) and (c), as the average bond number begins to rise above the rigidity percolation, the colloidal gel recovers its elasticity. This is expressed as a sudden increase of stress between the point (a) and 3 ((c) and 7).

The pair distribution functions in Figure. 5.2.3 show the change of structural anisotropy in the LAOS regime. The colloidal gel shows structural anisotropy quite similar with that observed in the MAOS regime. The increase in the absolute value of strain (from point 1 to 3 and from 5 to 7) induces structural anisotropy along the compressional axis, and the decrease in the absolute value of strain (from point 3 to 5 and from 7 to 1) by the reverse flow reduces structural anisotropy. However, compared to that of the MAOS, the colloidal gel shows more anisotropic structure in LAOS. In addition, due to the high shear rate flow, the string structure appears as has been observed previously in the works with hard spheres [63, 64, 66]. The formation of a string structure may be attributed to the neglect of hydrodynamic interaction. It means that the hydrodynamic interaction, which is ignored in this study, can be important even for the inter-particle force dominant system. In this sense, the role of hydrodynamic interaction needs to be studied further.

5.3. Stress analysis by stress decomposition method

From the Fourier transformation [73-75] to a recent work where the nonlinear behavior is considered as a sequence of physical processes [76, 77], diverse analysis methods have been proposed to interpret the nonlinear response of complex fluids. Among them, in the method with geometrical interpretation of the nonlinear behavior [78], the response of the material is studied by decomposing the stress signals to elastic and viscous components. In this study, we analyzed the nonlinear stress responses with the stress decomposition method, and associated it with the microstructural change of the colloidal gel.

Figure. 5.3.1 shows the stress decomposition and the Lissajous curves in each regime. In the first row, the results from the SAOS regime are presented. In the SAOS regime at a strain amplitude of 3%, the elastic stress shows a sinusoidal curve which is in phase with the strain. The viscous stress also shows a sinusoidal curve. This linear behavior is observed in the Lissajous plot as well. The elastic stress is represented by a straight line with a constant slope which reveals the characteristic feature of the linear behavior. In the MAOS regime at a strain amplitude of 15%, a linear- to-nonlinear transition is observed. In the second row of Figure. 5.3.1, the stress decomposition and the Lissajous curve in the MAOS regime are shown. In this regime, even though the viscous stress demonstrates a sinusoidal curve as in the SAOS regime, the elastic stress displays a deviation from the sinusoidal curve. Moreover, the elastic stress is not a straight line any more in the Lissajous curve. In the third row in Figure. 5.3.1, the stress decomposition and the Lissajous curve in the LAOS regime are shown. As in the MAOS regime, the elastic stress does not show the straight line, and the viscous stress is no longer elliptic, which indicates that the nonlinear behavior in the LAOS regime is attributed to both elastic and viscous stresses. The observed elastic stress can be closely correlated with the microstructure of the colloidal gel. Figure. 5.3.2 shows the normalized elastic stress ($\sigma_{elastic}/\sigma_{elastic\,max}$) at various strain amplitudes as

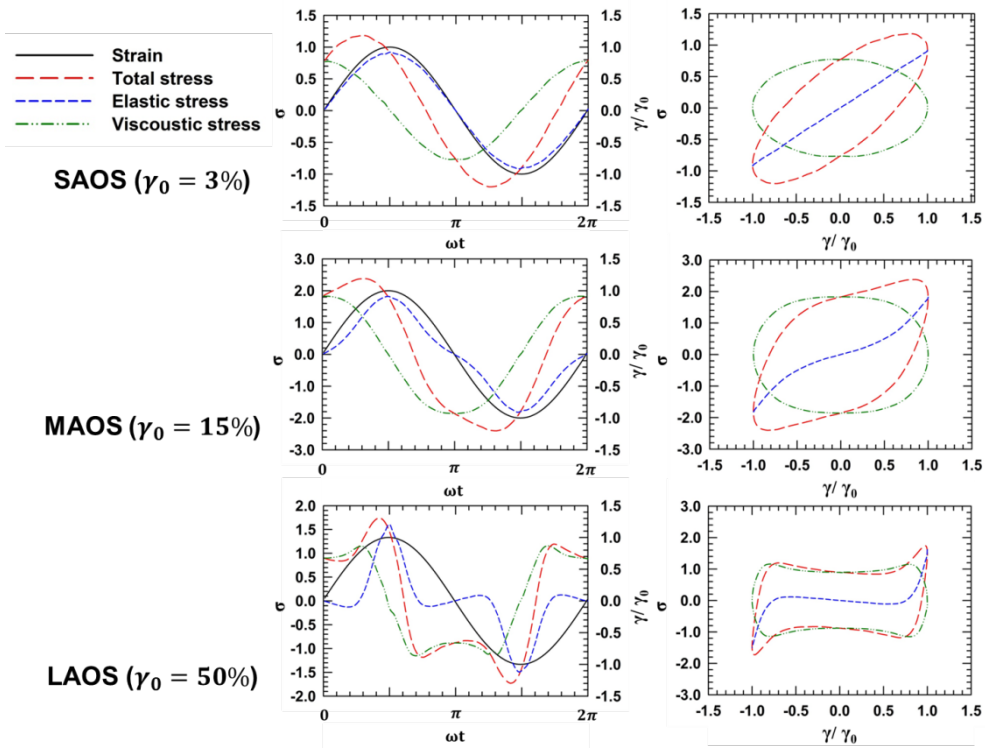

Figure. 5.3.1. Stress decomposition and Lissajous curves at three different regimes (SAOS, MAOS, LAOS).

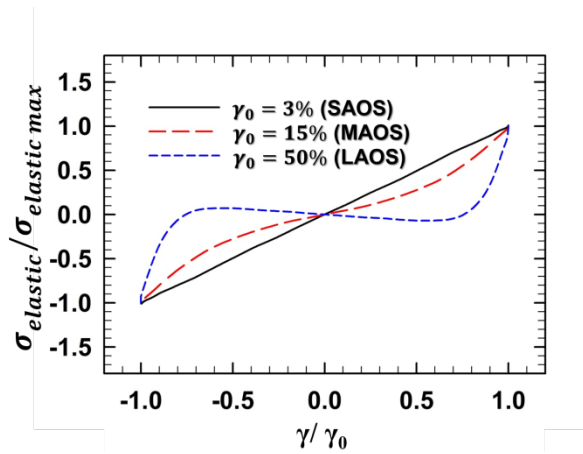

Figure. 5.3.2. Normalized elastic stress ($\sigma_{elastic}/\sigma_{elastic\ max}$) as a function of normalized strain (γ/γ_0).

a function of normalized strain (γ/γ_0). In the SAOS regime, the elastic stress is a straight line with a constant slope. The perfectly elastic behavior can be related to the rigid chain structure in the SAOS regime, where the network structure of the rigid chains is maintained. Because the rigid chain structure with high bond number is the origin of elasticity, the elastic stress which originates from the network of the rigid chains demonstrates the perfectly elastic behavior.

In the LAOS regime, where the colloidal gel consists of singly-connected soft chains, a different behavior is observed. In Figure. 5.3.2, the elastic stress is divided into two different parts. At large strain, the elastic stress is sensitive to the strain with a steep slope, which represents a strong elasticity. At small strain, the elastic stress shows a nearly plateau which indicates no elasticity. This result can be attributed to the soft chain structure in LAOS regime. According to the structural analysis, in the LAOS regime, the gel structure is ruptured and the initial rigid chain structure turns into the soft chain structure. Different from the rigid chain with high bond number, the soft chain with low bond number shows a floppy motion without resistance to deformation, and the colloidal gel shows no elasticity in the plateau region. However, as the strain increases further, the soft chain starts to stretch and break up at large strain. Therefore, the stretched soft chain, which is the most stress-bearing configuration [26, 28], demonstrates strong elasticity.

In the MAOS regime, the elastic behavior in between the SAOS and LAOS regime is observed. The elastic stress with strain amplitude of 15% shows two different behaviors. As in the LAOS regime, the colloidal gel shows relatively strong elasticity at large strain compared to small strain. However, unlike the LAOS regime where the elastic stress shows no elasticity at small strain, the elastic stress shows a weak elasticity with a mild slope at small strain. The slope is less steep than that in the SAOS regime. In previous section, it has been shown that some of the rigid chains are ruptured in the MAOS regime and the colloidal gel consists of both rigid and soft chains. At small strain, the remaining rigid network induces elastic behavior as in the SAOS regime. However, compared to the elasticity in the SAOS regime, it demonstrates the relatively weak elasticity due to

the rupture of some rigid chains. At large strain, as in the LAOS regime, the elasticity with a nonlinear increase of the elastic stress is observed. This strong elasticity can be thought to be originated from the stretching and breakup of the chain network structure of the colloidal gel.

So far, the stress responses of the colloidal gel in three regimes of SAOS, MAOS, and LAOS have been discussed with the stress decomposition method. However, it should be noted that there exists an argument whether the application of the stress decomposition to yielding systems is appropriate or not. For more clear understanding on the nonlinear response of this complex fluid system, more researches with various stress analysis techniques will be necessary [76-80].

Chapter 6. Conclusion

6. Conclusion

In this work, the coupling between the structural change and the rheology of colloidal gel has been studied by using the Brownian dynamics simulation method with surface bonding concept. It was studied under the flow conditions of the start-up shear and the dynamic oscillatory shear flow.

In the chapter 3, the structural evolution of colloidal gel was studied under the start-up shear flow. We could divide the structural evolution of colloidal gel into three regimes. In regime 1, colloidal gel was deformed and no significant structural change was observed. In this regime, the particles organized a percolated network structure. As the strain increased, in regime 2, the percolated network was fractured into several large clusters. The fractured clusters continuously decomposed into small flocs, reaching regime 3, the steady state. The rupture of the colloidal gel resulted in linear to non-linear transition represented by the change in the slope of the stress growth. We analyzed the structural evolution of the colloidal gel from different points of views; on cluster length scale, on local length scale and on anisotropy. On the cluster length scale, the mismatch between the initiation of the structural rupture and the stress maximum was observed. The mismatch was attributed to the competition between the structural rupture which decreases the stress and the deformation of the stress-bearing network structure which increases the stress. In this point of view, the stress maximum could be defined as the balance of this competition. On the local length scale, the topology of the colloidal gel was investigated by measuring the average bond number and the bond number distribution change. The topology change showed a strong tendency to lose rigidity with decrease in the number of particles with bond number higher or equal to 4, which corresponds to the experiment result of yielded colloidal gels. Therefore, on the local length scale, the structural evolution of the colloidal gel under shear flow could be regarded as a transition of the multiply-connected rigid chains to the singly-connected soft

chains, during which the rigidity, the origin of elasticity, was lost. In the structural analysis using pair distribution function, distinctive change in anisotropy was observed. Correlating the average bonding angle change with the three representative motions of the clusters, it was possible to propose a mechanism that the structural evolution proceeds in the sequence of deformation, break up of percolated network, rotation and break up of clusters, and equilibrium of the three representative motions of small flocs(break up, rotation, interlocking.)

In the chapter 4, the structural anisotropy of colloidal gel under start-up shear flow was studied more intensively and correlated to the stress responses. Under start-up shear flow, the colloidal gel shows structural anisotropy in the direction of the compressional axis and vorticity axis. The shear-induced structural anisotropy was analyzed in both real space and reciprocal space. In real space, pair distribution function and its spherical harmonics expansion were studied. In reciprocal space, structure factor was employed and the structural anisotropy was quantified through an alignment factor. The structure analysis showed that the structure in the vorticity direction undergoes less structural changes compared with the velocity direction and the gradient direction. The rupture being preferred in the extensional direction explained the evolution of the structural anisotropy. The result provides an insight into the role of the attractive force in the creating anisotropic structure along the vorticity direction. In this work, the correlation between the structural anisotropy and the rheological behavior was studied as well. The stress response of the colloidal gel under start-up shear flow was quantitatively linked to the structural anisotropy through spherical harmonic expansion of the pair distribution function and a stress-SANS rule. The theoretical prediction using the spherical harmonic expansion of the pair distribution function correctly caught the correlation between the correlation between the structural anisotropy and the stress response. However, the stress response calculated from the existing stress-SANS rule showed deviation from the measured stress, which can be attributed to the absence of the information on the size-related structure change. To overcome the limit, the stress-SANS rule was modified to include the influence of the structural

change under flow. The modified stress-SANS rule predicted the stress response correctly.

In the chapter 5, the structural changes, oscillating dynamics, and rheological behavior of a colloidal gel under oscillatory shear flow have been explored. The structural changes of the colloidal gel were quantified by the average bond number, and the oscillating dynamics was studied by investigating the structural fluctuation of the colloidal gel which was quantified by the change of average bond number. The rheological behavior was analyzed by the stress decomposition method. According to the flow conditions, different microstructural changes of the colloidal gel were observed. As the strain amplitude increased, the rigid chain structure with high bond number changed into soft chain structure with low bond number. The characteristic microstructure at each regime manifested itself in the distinctive oscillating dynamics and rheological behavior. In the SAOS regime where the network structure with rigid chains was retained, the colloidal gel showed the oscillating dynamics with no remarkable structural fluctuation. Although the average bond number showed a negative correlation with the absolute value of strain, no significant variation of the average bond number was observed during the oscillation. The maintained network structure with rigid chain represented linear rheological behavior. In the MAOS regime, the rupture of the colloidal gel was observed. The structural change from rigid to soft chains started in this regime, however, the overall structure was still dominated by rigid chains with high bond number. Under oscillatory shear flow, the average bond number decreased with the increase in the absolute value of strain and the average bond number increased with the decrease in the absolute value of strain. The negative correlation between the absolute value of strain and the average bond number could be attributed to the characteristic dynamics of the rigid chains which resists against deformation. In this regime, a linear-to-nonlinear transition, represented by the non-sinusoidal stress curve, was observed. The colloidal gel showed elastic behavior in between the SAOS and LAOS regime. In the LAOS regime, the colloidal gel showed the microstructure with soft chains. Most of the rigid chain structure ruptured into the

singly-connected soft chains which do not resist deformation. Under the oscillatory shear flow, the average bond number increased with the increase in the absolute value of strain and decreased with the decrease in the absolute value of strain. The oscillating dynamics with a positive correlation between the absolute value of strain and the average bond number, which is significantly different from that in previous two regimes, was correlated with the floppy motion of the soft chains. In this regime, both elastic and viscous stresses reflected highly nonlinear rheological behavior. Because of the soft chain structure without elasticity, the elastic stress exhibited no elasticity at small strain. At large strain, the stretching of the soft chain structure induced strong elasticity.

References

References

1. P. Meakin, Formation of fractal clusters and networks by irreversible diffusion limited aggregation, *Phys. Rev. Lett*., 1983, **51**, 1119

2. D. A. Weitz, M. Oliveria, Fractal structures formed by kinetic aggregation of aqueous gold colloids, *Phys. Rev. Lett*., 1984, **52**, 1433

3. C. M. Sorensen, A. Chakrabarti, The sol to gel transition in irreversible particulate systems, *Soft Matter*, 2011, **7**, 2284

4. W. H. Shih, W. Y. Shih, S. I. Kim, J. Liu, I. A. Aksay, Scaling behavior of the elastic properties of colloidal gels, *Phys. Rev. A*, 1990, **42**, 4772

5. N. Koumakis, M. Laurati, S. U. Egelhaaf, J. F. Brady, G. Petekidis, Yielding of hrad-sphere glasses during start-up shear, *Phys. Rev. Lett*., 2012, **108**, 098303

6. L. J. Kaufman, D. A. Weitz, Direct imaging of repulsicve and attractive colloidal glasses, *J. Chem. Phys*., 2006, **125**, 074716

7. D. Potoni, T. Narayanan, J. M. Petit, G. Grubel, D. Beysens, Microstructure and dynamics near an attractive colloidal glass transition, *Phys. Rev. Lett*., 2003, **90**, 188301

8. K. Masschaele, J. Fransaer, J. Vermant, Direct visualization of yielding in model two-dimensional colloidal gels subjected to shear flow, *J. Rheol*., 2009, **53**, 1438

9. M. H. Lee, E. M. Furst, Response of a colloidal gel to a microscopic oscillatory strain, *Phys. Rev .E*, 2008, **77**, 041408

10. P. J. Lu, E. Zaccarelli, F. Ciulla, A. B. Schofield, F. Sciortino, D. A. Weitz, *Nature*, 2008, **453**, 499

11. C. J. Dibble, M. Kogan, M. J. Solomon, Structure and dynamics of colloidal depletion gels: Coincidence of transitions and heterogeneity, *Phys. Rev .E*, 2006, **74**,041403

12. F. Cardinaux, T. Gibaud, A. Stradner, P. Schurtenberger, Interplay between spinodal decomposition and glass formation in proteins exhibiting short-range attractions, *Phys. Rev. Lett*., 2007, **99**, 118301

13. C. P. Royall, S. R. Williams, T. Ohtsuka, H. Tanaka, Direct observation of a local structural mechanism for dynamic arrest, *Nature Mater*., 2008, **7**, 556

14. A. I. Campbell, V. J. Anderson, J. S. van Duijneveldt, P. Bartlett, Dynamical arrest in attractive colloids: The effect of long-range repulsion, *Phys. Rev. Lett*., 2005, **94**, 208301

15. M. van Hecke, Jamming of soft particles : geometry, mechanics, scaling and isostaticity, *J. Phys.: Condens. Matter*, 2010, **22**, 033101

16. M. Wyart, H. Liang, A. Kabla, L. Mahadevan, Elasticity of floppy and stiff random networks, *Phys. Rev. Lett*., 2008, **101**, 215501

17. A.A. Potanin, R. De Rooij, D. Van den Ende, J. Mellema, Microrhological modeling of weakly aggregted dispersions, *J. Chem. Phys*., 1995, **102**, 5845

18. A. D. Dinsmore, V. Prasad, I. Y. Wong, D. A. Weitz, Microscopic structure and elasticity of weakly aggregated colloidal gels, *Phys. Rev. Lett*., 2006, **96**, 185502

19. L. C. Hsiao, R. S. Newman, S. C. Glotzer, M. J. Solomon, Role of isostaticity and load bearing microstructure in the elasticity of yielded colloidal gels, *PNAS*, 2012, **109**, 16029

20. J. D. Park, K. H. Ahn, Structural evolution of colloidal gels at intermediate volume fraction under start-up shear flow, *Soft Matter*, 2013, **9**, 11650

21. R. N. Zia, B. J. Landrum, W. B. Russel, A micro-mechanical study of coarsening and rheology of colloidal gels : cage building, cage hopping, and smoluchoski's ratchet, *J. Rheol*., 2014, **58**, 1121

22. L. C. Hsiao, M. J. Solomon, K. A. Whitaker, E. M. Furst, A model colloidal gel for coordinated measurements of force, structure, and rheology, *J. Rheol*., 2014, **58**, 1485

23. J. Vermant, M. J. Solomon, Flow-induced structure in colloidal suspensions, *J. Phys.: Condens. Matter*, 2005, **17**, R187

24. K. Masschaele, J. Fransaer, J. Vermant, Flow-induced structure in colloidal gels: direct visualization of model 2D suspensions, *Soft Matter*, 2011, **7**, 7717

25. N. Koumakis, G. Petekidis, Two step yielding in attractive colloids, *Soft Matter*, 2011, **7**, 2456

26. B. Rajaram, A. Mohraz, Microstructural response of dilute colloidal gels to nonlinear shear deformation, *Soft Matter*, 2010, **6**, 2246

27. A. Mohraz, M. J. Solomon, Orientation and rupture of fractal colloidal gels during start-up shear of steady shear flow, *J. Rheol*., 2005, **49**, 657

28. J. Colombo, E. Del Gado, Stress localization, stiffening, and yielding in a model colloidal gel, *J. Rheol*., 2014, **58**, 1089

29. H. K. Chan, A. Mohraz, *Phys. Rev .E*, 2012, **85**,041403

30. M. Whittle, E.Dickinson, Large deformation rheological behavior of a model particle gel, *J. Chem. Soc., Faraday Trans*., 1998, **94**, 2453

31. A. A. Rzepiela, J. H. J. van Opheusden, Large shear deformation of particle gels studied by Brownian dynamics simulation, *J. Rheol*., 2004, **48**, 863

32. A. Mohraz, M. J. Solomon, The shear distorted microstructure of adhesive

hard sphere dispersions, *J. Rheol*., 1993, **37**, 71

33. P. Varadan, M. J. Solomon, Shear-induced microstructural evolution of a thermoreversible colloidal gel, *Langmuir*, 2001, **17**, 2918

34. H. Hoekstra, T. Narayanan, J. Mewis, J. Vermant, Multi length scale analysis of the microstructure in sticky sphere dispersions during shear flow, *Langmuir*, 2005, **21**, 11017

35. A. R. Eberle, N. Martys, L. Porcar, S. R. Kline, W. L. George, J. M. Kim, P. D. Butler, N. J. Wagner, *Phys. Rev .E*, 2014, **89**,050302(R)

36. J. M. Kim, A. R. Eberle, A. K. Gurnon, L. Porcar, N. J. Wagner, The microstructure and rheology of a model, thixotropic nanoparticle gel under steady shear and large amplitude oscillatory shear (LAOS), *J. Rheol*., 2014, **58**, 1301

37. H. Hoekstra, J. Vermant, J. Mewis, Flow induced anisotropy and reversible aggregation in two dimensional suspensions, *Langmuir*, 2003, **19**, 9134

38. X. Cheng, X. Xu, S. A. Rice, A. R. Dinner, I. Cohen, Role of isostaticity and load bearing microstructure in the elasticity of yielded colloidal gels, *PNAS*, 2012, **109**, 63

39. K. Hyun, M. Wilhelm, C. O. Klein, K. S. Cho, J. G. Nam, K. H. Ahn, S. J. Lee, R. H. Ewoldt, G. H. McKinley, A review of nonlinear oscillatory shear tests analysis and application of large amplitude oscillatory shear, *Prog. Polym. Sci*., 2011, **36**, 1697

40. J. T. Kim, A. D. Merger, M. Wilhelm, M. E. Helgeson, Microstructure and nonlinear signatures of yielding in a heterogeneous colloidal gel under large amplitude oscillatory shear, *J. Rheol*., 2014, **58**, 1359

41. P. A. Smith, G. Petekidis, S. U. Egelhaaf, W. C. K. Poon, Yielding and crystallization of colloidal gels under oscillatory shear, *Phys. Rev .E*, 2012,

76,041402

42. A. Satoh, *Introduction to Molecular-Microsimulation of Colloidal Dispersions*, Elsevier, Amsterdam, 2003

43. M. Allen and D. Tildesley, *Computer Simulation of liquids*, Oxford University Press, Oxford, 1987

44. M. Whittle, E.Dickinson, Brownian dynamics simulation of gelation in soft sphere systems with irreversible bond formation, *Mol. Phys*., 1997, **90**, 739

45. M. Whittle, E.Dickinson, Stress overshoot in a model particle gel, *J. Chem. Phys*., 1997, **107**, 10191

46. W. B. Russel, D. A. Saville, and W. R. Schowalter, *Colloidal Dispersions*, Cambridge University Press, Cambridge, 1989

47. J. H. Irving, J. G. Kirkwood, The statistical mechanical theory of transport process. Ⅳ. The equations of hydrodynamics, *J. Chem. Phys*., 1950, **18**, 817

48. J. S. Dahler, L. E. Scriven, Angular momentum of continua, *Nature*, 1961, **192**, 36

49. H. J. M. Hanley, J. C. Rainwater, S. Hess, Shear induced angular dependence of the liquid pair correlation function, *Phys. Rev. A*, 1987, **36**, 1795

50. L. M. Walker, N. J. Wagner, SANS analysis of the molecular order in poly/Deuterated Dimethylformamide under shear and during relaxation, Macromolecules, 1996, **29**, 2298

51. M. T. A. Bos, J. H. J. van Opheusden, Brownian dynamics simulation of gelation and aging in interacting colloidal systems, *Phys. Rev .E*, 1996, **53**,

5044

52. M. Mellema, J. H. J. van Opheusden, T. van Vliet, Relating colloidal particle interactions to gel structure using Brownian dynamics simulations and the Fuch stability ratio, *J. Chem. Phys*., 1999, **111**, 6129

53. P. Coussot, Rheophysics of pastes; a review of microscopic modelling approaches, *Soft Matter*, 2007, **3**, 528

54. Y. Kantor, I. Webman, Elastic properties of random percolating systems, *Phys. Rev. Lett*., 1984, **52**, 1891

55. A. D. Dinsmore, D. A. Weitz, Direct imaging of three-dimensional structure and topology of colloidal gels, *J. Phys.: Condens. Matter*, 2002, **14**, 7581

56. K. Dullaert, J. Mewis, A structural kinetics model for thixotropy, *J. Non-Newtonian Fluid Mech*., 2006, **139**, 21-30

57. M. Doi, D. Chen, Simulation of aggregating colloids, *J. Chem. Phys*., 1989, **90**, 5271

58. D. Chen, M. Doi, Microstructure and viscosity of aggregating colloids under strong shear force, *J. Colloid Interface Sci*., 1999, **212**, 286

59. R. Wessel, R. C. Ball, Fractal aggregates and gels in shear flow, *Phys. Rev. A*, 1992, **46**, R3008

60. P. Solich, F. Lequeux, P. Hebraud, M. E. Cates, Rheology of soft glassy materials, *Phys. Rev. Lett*., 1997, **78**, 2020

61. P. Solich, Rheological constitutive equation for a model of soft glassy materials, *Phys. Rev .E*, 1998, **58**, 738

62. S. M. Fielding, P. Solich, M. E. Cates, Aging and rheology in soft materials, *J. Rheol*., 2000, **44**, 323

63. D. R. Foss, J. F. Brady, Structure, diffusion, and rheology of Brownian suspensions by Stokesian Dynamics simulation, *J. Fluid Mech*., 2000, **407**,167

64. J. F. Morris, B. Katyal, Microstrucrure from simulated Brownian suspension flows at large shear rate, *Phys. Fluid*, 2002, **14**, 1920

65. A. K. Gurnon, N. J. Wagner, Microstructure and rheology relationship for shear thickening colloidal dispersions, *J. Fluid Mech*., 2015, **79**, 242

66. B. Xu, J. F. Gilchrist, Microstructure of sheared monosized colloidal suspensions resulting from hydrodynamic and electrostatic interactions, *J. Chem. Phys*., 1950, **18**, 817

67. S. Hess, H. J. M. Hanley, Pressure tensor and viscosity coefficients of a soft sphere liquid under shear, *Intl J.of Thermophysics*. 1983, **4**, 97

68. M. E. Helgeson, , P. A. Vasquez, E. W. Kaler, N. J. Wagner, Rheology and spatially resolved structure of cetyltrimethylammonium bromide wormlike micelles through the shear banding transition, *J. Rheol*., 2009, **53**, 727

69. A. K. Gurnon, C. R. Lopez-Barron, A. R. Eberle, L. Porcar, N. J. Wagner,, Spatiotemporal stress and structure evolution in dynamically sheared polymer-like micellar solutions, *Soft Matter*, 2014, **10**, 2889

70. A. K. Gurnon, C. R. Lopez-Barron, M. J. Wasbrough, L. Porcar, N. J. Wagner, Spatially resolved concentration and segmental flow alignment in a shear-banding solution of polymer-like micelles, *ACS Macro let*., 2014, **3**, 276

71. H. He, M. F. Thorpe, Elastic properties of glasses, *Phys. Rev. Lett*., 1985, **54**, 2107

72. N. E. Valadez-Perez, Y. Liu, A. P. R. Eberle, N. J. Wagner, R. Castaneda-Priego, Dynamical arrest in adhesive hard-sphere dispersions driven by

rigidity percolation, *Phys. Rev .E*, 2013, **88**, 060302

73. M. Wilhelm, D. Maring, H. W. Spiess, Fourier Transform rheology, *Rheol. Acta.*, 1998, **35**, 399

74. K. Hyun, W. Kim, A new non-linear parameter Q from FT-rheology under nonlinear dynamic oscillatory shear for polymer melts system, *Korea-Aust. Rheol. J.*, 2011, **23**, 227

75. M. Wilelm, Fourier-Transform rheology, *Macromol. Mater. Eng.*, 2002, **287**, 83

76. S. A. Rogers, B. M. Erwin, D. Vlassopoulos, M. Cloitre, A sequence of physical processes determined and quantified in LAOS : Application to a yield stress fluid, *J. Rheol.*, 2011, **55**, 435

77. S. A. Rogers, M. P. Lettinga, A sequence of physical processes determined and quantified in LAOS : Application to theoretical nonlinear models, *J. Rheol.*, 2012, **56**, 1

78. K. S. Cho, K. H. Ahn, S. J. Lee, A geometrical interpretation of large amplitude oscillatory shear response, *J. Rheol.*, 2005, **49**, 747

79. A. S. Poulos, J. Stellbrink, G. Petekidis, *Rheol. Acta.*, 2013, **52**, 785

80. R. H, Ewoldt, A. E. Hosoi, G. H. McKinley, New measures for characterizing nonlinear viscoelasticity in large amplitude oscillatory shear, *J. Rheol.*, 2008, **52**, 1427

국문 초록

국문초록

콜로이드 입자는 탄성이나 전기 전도성과 같은 재료의 특성을 급격히 변화시킬 수 있기 때문에, 자연과학 및 산업 전반에 걸쳐서 매우 중요한 역할을 한다. 대부분의 경우 이러한 재료 특성의 변화는 콜로이드 입자들이 만들게 되는 독특한 내부 구조에 기인한다. 가장 대표적인 예로 콜로이드 젤을 생각해 볼 수 있다. 충분히 높은 농도에서, 입자 상호간의 인력을 통해서 상호작용하는 입자들은 재료 전체에 걸쳐서 퍼져있는 네트워크 구조를 형성하게 된다. 이러한 네트워크 구조는 콜로이드 젤이라고 불린다. 콜로이드 입자가 젤 구조를 형성하는 과정은 다양한 콜로이드 시스템에서 관찰된다. 콜로이드 젤은 고체 같은 물리적 성질을 통해서 특징지어진다. 이러한 고체와 같은 물성은 입자들이 이루고 있는 불규칙한 고체 구조로 인해서 발생된다. 그러한 구조는 주변입자들과의 상호작용에 의한 인력으로 움직임이 방해되는 입자들의 동역학적 특성에 기인한다. 입자들의 미세 네트워크 구조의 형성에 의해서 콜로이드 젤은 다양한 특성을 보이게 된다. 그러나 이러한 콜로이드 젤의 특성은 아직까지 충분히 이해되지 않았다.

충분히 큰 변형이나 힘이 가해질 경우, 콜로이드 젤 내부의 네트워크 구조는 깨어지게 된다. 그와 동시에 다양한 비선형적인 유변거동을 동반하는 non-Newtonian 유체의 특성을 보이며 흐르게 된다. 이러한 콜로이드 젤 내부 구조의 붕괴는 Yielding 이라고 불린다. 콜로이드 젤의 Yielding 거동은 구조의 재배치, 입자간 결합 파괴, cage breakage, 구조적 비등방성 등의 형태로 나타나게 된다. 콜로이드 젤의 Yielding 거동을 이해하기 위해서 Light scattering 에서부터 Computer simulation 까지 다양한 실험적, 이론적 연구가 이루어져 왔다. 그러나 이러한 수많은 연구에도 불구하고, 콜로이드 젤의 Yielding 거동은

제대로 이해되지 못하고 있다. 특히 콜로이드 젤의 Yielding 거동의 근본적인 발생기제에 대한 이해가 부족하다.

외력을 견디는 네트워크 구조 붕괴와 같은 다양한 형태의 구조변화로 나타나는 yielding 거동은 콜로이드 젤의 stress response 에 큰 영향을 끼치게 된다. Yielding 으로 비롯된 복잡한 구조 변화들은 yield stress 나 non-linear creep compliance 와 같은 다양한 비선형 유변학적 거동으로 나타나게 된다. 콜로이드 젤의 미세구조와 유변학적 거동이 밀접한 관련이 있음을 고려해 볼 때, 콜로이드 젤의 미세구조 변화를 특징지어 이해하는 것은 콜로이드 젤의 비선형 유변학적 거동을 이해하는데 있어서 필수적이라고 할 수 있다. 따라서 비선형 유변학적 거동의 근본원리에 대한 연구는 미세구조와 유변 특성 사이의 상호관계를 연구하는 방식으로 이루어져 왔다. 이러한 미세구조와 유변 물성사이의 상호관계 연구는 유변학 분야에서 가장 중요한 과제라고 볼 수 있다.

일반적으로 미세구조와 유변 물성 사이의 상호관계는 start-up shear flow 및 dynamics oscillatory shear flow 하에서 연구된다. 이러한 유동조건을 이용한 실험적 연구에서는 유변물성 측정 장치를 이용해서 측정된 stress response 를 direct visualization 이나 scattering 방법론 등을 이용해서 측정된 콜로이드 젤의 구조 변화 정보에 연관 시키는 방식으로 연구가 진행되어 왔다. 그러나 이러한 연구는 몇몇 특정한 실험 조건에 제한되게 된다. 또한 구조의 관찰을 어렵게 하는 다양한 실험적 어려움이 존재한다. 이러한 실험적 연구의 한계에 대한 대안으로서 입자 시뮬레이션 방법론을 이용한 이론적 연구를 생각해 볼 수 있다. 몇 가지 측면에서 입자 시뮬레이션 방법론을 이용한 이론적 연구는 실험적 연구에 비해서 장점을 가지게 된다. 입자 시뮬레이션을 이용한 연구의 경우 입자의 위치 또는 입자에 가해지는 힘이나 토크와

같은 모든 물리적 정보를 정확하게 알 수 있기 때문이다. 특히 입자 시뮬레이션 가운데에서도 Brownian dynamics simulation 방법론의 경우, 콜로이드 젤이나 글래스와 같이 입자간의 상호작용이 지배적인 콜로이드 시스템의 중요한 물리적 현상들을 잘 묘사하기 때문에 널리 사용되어 왔다.

본 연구의 목표는 Brownian dynamics simulation 방법론을 이용해서 콜로이드 젤의 미세구조와 유변 물성 사이의 상호관계를 연구하는 것이다. 본 연구에서는 start-up shear flow 및 dynamic oscillatory shear flow 조건에서 콜로이드 젤의 미세구조변화와 동역학을 분석 할 것이다. 콜로이드 젤의 구조변화는 모든 입자들의 위치 및 물리 정보를 정확하게 알 수 있는 시뮬레이션 방법론의 장점을 이용해서 서로 다른 다양한 관점에서 분석될 것이다. 관찰된 콜로이드 젤의 동역학 및 구조변화는 통계역학적인 방법론들을 이용해서 해석될 것이며, 유변학적 거동과 연관되어 설명될 것이다. 본 연구의 결과는 콜로이드 젤의 yielding 및 그와 관련된 비선형적 유변학적 거동의 이해를 도울 것이다.

주요어: 콜로이드 젤, 진동전단유동, 브라운 역학 시뮬레이션, 작은 진폭 진동전단유동, 중간 진폭 진동전단유동, 큰 진폭 진동전단유동, 구조적 비등방성.

학번 : 2010-20991